Long-range interacting many-body systems in the irrep basis

Ivy Pannier-Günther [1,*] Andrew Kolmer Forbes,[1,†] Pablo M. Poggi [1,2] and Ivan H. Deutsch [1]
[1]Center for Quantum Information and Control, Department of Physics and Astronomy, University of New Mexico, Albuquerque, New Mexico 87131, USA
[2]Department of Physics, SUPA and University of Strathclyde, Glasgow G4 0NG, United Kingdom

(Received 14 May 2025; accepted 16 September 2025; published 15 October 2025)

Spin models featuring infinite-range, homogeneous all-to-all interactions can be efficiently described due to the existence of a symmetry-restricted Hilbert subspace and an underlying classical phase-space structure. However, when the permutation invariance of the system is weakly broken, such as by long- but finite-range interactions, these tools become mathematically invalid. Here, we propose to approximately describe these scenarios by considering additional many-body subspaces according to the hierarchy of their coupling to the symmetric subspace, defined by leveraging the structure of irreducible representations (irreps) of the group $SU(2)$. We put forward a procedure, dubbed "irrep distillation," which defines these additional subspaces to minimize their dimension at each order of approximation. We discuss the validity of our method in connection with the occurrence of quantum many-body scars, benchmark its utility by analyzing the dynamical and equilibrium phase transitions, outline its phenomenology, and compare its use-cases against other approximations of long-range many-body systems.

DOI: 10.1103/w12m-9f2s

I. INTRODUCTION

The complexity of quantum many-body systems is of interest from both natural and computation perspectives. The mathematical description of such complex systems depends strongly on the range of the interactions, from infinite-range all-to-all couplings as in the Lipkin-Meshkov-Glick (LMG) model [1] and Tavis-Cummings Hamiltonian [2], to nearest-neighbor interactions such as those in the PXP Hamiltonian [3,4] and standard Ising models [5]. In each of these two extremes, there are geometries for which analytic simplifications permit exact solutions, even at large system sizes. However, for long, but not infinite-range multibody interactions, the lack of symmetry typically eludes integrability and confounds most exact solving techniques. The goal of this work is to develop tools to describe these long-range quantum many-body systems and broaden our understanding of the resulting phenomenology.

The range-dependent behavior of quantum many-body physics is especially evident in spin systems as exemplified by the one-dimensional (1D) transverse-field Ising model, which is integrable for infinite-range and zero-range (nearest-neighbor) models, but not integrable elsewhere. Permutation-symmetric spin Hamiltonians, in the limit of infinite-range interactions, reduce to collective-spin models representing a single-body degree of freedom and a block-diagonal Hamiltonian that strongly constrains the dynamics. However, any violation of permutation symmetry explodes the dynamically accessible Hilbert space and renders the system irreducibly many body in description. In many cases, the finite range of interactions is accompanied by a collapse of integrable dynamics into nonintegrability and even chaos; the transverse-field Ising model is known to be chaotic in this regime [6,7]. While exact integrability can be lost, perturbation theory informs us that sufficiently minor deviations from infinite-range interactions at finite system sizes should still approximate their collective counterparts' dynamics, especially in terms of collective observables like net polarization, spin number, and entanglement quantifiers. Likewise, reduced-state evolution on finite subsystems in long-range systems are independent of local interactions [8].

The near integrable behavior of long-range (but not infinite-range) Ising models under specific initializations was elucidated in recent theoretical developments by Lerose *et al.* [9], who explained the retention of collective dynamical order by characterizing the subset of eigenstates responsible for high cooperativity. The strong/weak eigenstate thermalization hypothesis (ETH) predicts that all (strong) or nearly all (weak) eigenstates of chaotic Hamiltonians should be indistinguishable from thermal states according to local measurements [10], and the vanishing fraction of eigenstates, which violate the strong ETH are called quantum many-body scars (QMBS) [11,12]. Lerose *et al.* demonstrated generic QMBS across a wide class of long-range time-independent spin Hamiltonians; these QMBS are characterized by low entanglement entropy, high spin number, and a high spectral gap between each scar state and neighboring eigenstates outside the QMBS. In the limit of infinite-range interactions, the QMBS reduces to the permutation-symmetric eigenstates of the corresponding collective system.

*Contact author: igunther@unm.edu
†Contact author: aforbes@unm.edu

Published by the American Physical Society under the terms of the Creative Commons Attribution 4.0 International license. Further distribution of this work must maintain attribution to the author(s) and the published article's title, journal citation, and DOI.

In this work, we consider a scheme of approximation for long-range interacting spin Hamiltonians, which generates a perturbation-theoretic QMBS. By extending the corresponding subspace from the collective system using $\mathcal{O}(N)$ matrix elements in an efficient basis, we exploit an alternative representation of the Hilbert space, not as a tensor product of N spin-1/2 particles, but as a *direct sum of degenerate irreducible representations of* $SU(2)$. We analytically "distill" these irreducible representations to truncate the Hilbert space down to the nondegenerate minimal subspace necessary to obtain the long-range system as a first-order perturbation on the infinite-range system.

This article is organized as follows. In Sec. II, we establish the foundational formalism, including a description of the system of interest, a transverse Ising model with tunable interaction strength and range, which generically exhibits chaos and QMBS. Here, we define the decomposition of Hilbert space into irreducible representations of $SU(2)$. By constructing the Hamiltonian in this basis, we observe patterns in its block structure, which motivates Hilbert space truncation using an efficient approximation scheme, which we dub irrep distillation. In Sec. III, we apply this formalism in various applications, including a detailed discussion of QMBS, dynamical quantum phase transitions (DQPTs), and the study of the dynamics of nonclassical states, going beyond what is possible with semiclassical approaches. In Sec. IV, we further explicate the special features of our formalism, defining its niche among the canonical approximations of long-range many-body systems. We explain the unique tensor product structure afforded by irrep distillation, which allows us to describe long-range many-body systems as consisting of two degrees of freedom, thereby generalizing the single-body collective spin description of infinite-range systems. We summarize and provide an outlook for future studies in Sec. V.

II. FORMALISM

A. Model

We consider a class of Ising Hamiltonians with power-law decaying longitudinal interactions and a symmetric transverse field parametrized as

$$\hat{H}(s,\alpha) = \frac{s-1}{2}\sum_{j=1}^{N}\hat{\sigma}_x^{(j)} - \frac{s}{4\mathcal{N}}\sum_{j,k=1}^{N}\frac{\hat{\sigma}_z^{(j)}\hat{\sigma}_z^{(k)}}{|j-k|^{\alpha}}. \tag{1}$$

We denote the relative strength of the interactions over the field by a single parameter $s \in [0,1]$, to ensure constant energy scale $||\hat{H}||$ for all parameter values. The parameter $\alpha \in [0,\infty)$ describes the power-law decay, or the range of the interactions, and we further guarantee energy scale invariant to α by normalizing with $\mathcal{N} \equiv \frac{1}{N-1}\sum_{j,k}|j-k|^{-\alpha}$, the Kac normalization [13]. Thus, we have extensive energy scaling with system size N, and otherwise totally invariant to parameters. We consider open boundary conditions as opposed to periodic, both for its experimental feasibility and because numerous analyses of long-range spin systems have exploited the translation invariance afforded by periodic boundaries, leaving a gap in the literature for solutions, which tolerate open boundary edge effects. This model arises naturally in ion traps [14] and Rydberg atom arrays [15] with Van der Waals and dipole-dipole interactions, and many-body dynamics for such long-range interacting systems have been studied in a variety of applications [16–21].

In the limit $\alpha \to 0$, Eq. (1) reduces to an LMG model [1],

$$\begin{aligned}\hat{H}(s,0) &= \frac{s-1}{2}\sum_j \hat{\sigma}_x^{(j)} - \frac{s}{4N}\sum_{j,k}\hat{\sigma}_z^{(j)}\hat{\sigma}_z^{(k)} \\ &= (s-1)\hat{J}_x - \frac{s}{N}\hat{J}_z^2,\end{aligned} \tag{2}$$

where

$$\hat{J}_\gamma = \frac{1}{2}\sum_{i=1}^{N}\hat{\sigma}_\gamma^{(i)} \tag{3}$$

are the components of the collective spin angular momentum satisfying the usual $SU(2)$ commutation relations. In the case of Eq. (2), the system commutes with total angular momentum $[\hat{H}(s,0),\hat{J}^2]=0$, and so the LMG eigensystem has the following quantum numbers:

$$\hat{H}(s,0)|n\rangle = E_n|n\rangle, \tag{4}$$

$$\hat{J}^2|n\rangle = J_n(J_n+1)|n\rangle. \tag{5}$$

That the energy eigenstates are jointly eigenstates of a global operator brings analytical benefits through the expression of the Hamiltonian in the corresponding basis of collective states. This natural basis, in fact, is the Dicke basis, which decomposes into irreducible representations of $SU(2)$, which we will discuss in the next section.

The transverse-field Ising model exhibits quantum phase transitions (QPTs) between ferromagnetic and paramagnetic phases defined by order parameters in the ground state [22] and through dynamical order parameters associated with time-averaged correlation functions [20,23,24]. For all-to-all symmetric interactions such as the LMG model, the thermodynamic limit ($N \to \infty$) of phase transitions is equivalent to the mean-field description [25]. This is seen in the classical phase space (θ,ϕ) of the sphere, where the mean-field LMG is described by classical energy function,

$$\begin{aligned}E(s;\theta,\phi) &= \langle\theta,\phi|\hat{H}(s,0)|\theta,\phi\rangle \\ &= (s-1)\sin\theta\cos\phi - \frac{s}{2}\cos^2\theta,\end{aligned} \tag{6}$$

where $|\theta,\phi\rangle = e^{-i\phi\hat{J}_z}e^{-i\theta\hat{J}_y}|\uparrow\rangle^{\otimes N}$ is a spin-coherent state (SCS). For small s, this forms a single well centered on $(\theta,\phi)=(\frac{\pi}{2},0)$ as in Fig. 1, but as s grows to $s_{\mathrm{GQPT}}=1/2$, this well undergoes a pitchfork bifurcation, splitting into a double well with a separatrix between, and $(\frac{\pi}{2},0)$ becomes an unstable fixed point on the separatrix. Any point initialized below the separatrix energy will be bound to one well; any point above will orbit around both (shown in Fig. 1). These two orbits can be distinguished in the thermodynamic limit by the order parameter of Z polarization, $\langle J_z\rangle$. The ground-state quantum phase transition (GQPT) corresponds to spontaneous symmetry breaking of the ground state at the critical value $s_{\mathrm{GQPT}}=1/2$, and so the GQPT is a kinematic property of the LMG's eigensystem. An order parameter for DQPT corresponds to the long time-average of the Z polarization, $\overline{\langle J_z(t)\rangle}$ after quench dynamics, with the state initialized

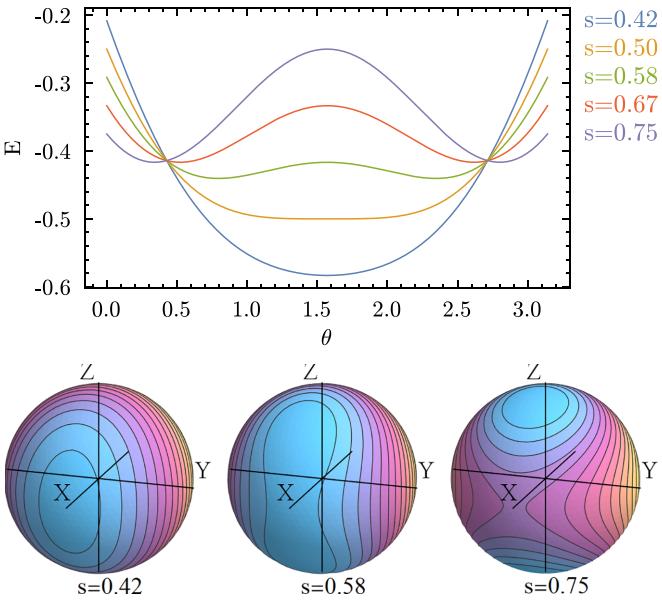


FIG. 1. The energy function $E(s;\theta,\phi)$ of the collective spin LMG, from Eq. (6), depicted in cross section at $\phi = 0$, which governs the mean-field dynamics. The bifurcation of the single well to a double well gives rise to a GQPT at the critical points $s_{\mathrm{GQPT}} = 1/2$ and a DQPT as $s_{\mathrm{DQPT}} = 2/3$. Below, the energy function on the sphere, showing the split of the single-well potential into two wells an corresponding mean-field paramagnetic/ferromagnetic phases.

in a Z-polarized SCS [26]. In the thermodynamic limit, when $s = s_{\mathrm{DQPT}} = 2/3$, then the initial SCS lies on the separatrix, and this determines the DQPT critical point [27].

Even without perfect permutation symmetry, $\hat{H}(s,\alpha)$ still obeys two other symmetries: global spin-flip parity and permutative mirror symmetries. That is, the global spin-flip operator $\exp(i\pi \sum_j \hat{\sigma}_x^{(j)})$ commutes with the Hamiltonian, and under the spin-site relabeling $j \to N+1-j$, the Hamiltonian is unchanged. Finally, the dynamics of $\hat{H}(s \approx 0,\alpha)$ is only perturbed slightly from simple Larmor precession generated by $\hat{J}_x$ for s small. On the other hand, while $\hat{H}(s=1,\alpha)$ is a long-range one-axis-twisting model with integrable dynamics [28]. This integrability arises from severe degeneracies in the spectrum, which immediately break upon the introduction of even a minuscule transverse field. For this reason, the chaos in $\hat{H}(s \approx 1,\alpha)$ does not resemble dynamics from $\hat{H}(s=1,\alpha)$.

B. Irreducible representations

As the interaction becomes finite but long-range ($0 < \alpha \lesssim 2$) [19], we expect some preservation of collective dynamics. Central to our method, thus, is to organize Hilbert space according to a notion of the collective order, by leveraging irreducible representations of $SU(2)$. An irreducible representation (irrep) of $SU(2)$ is a nonzero representation that cannot be broken down into smaller, nontrivial subrepresentations. In standard parlance, an irrep can be used to denote a subspace of the vector space that is closed under ladder operators $\hat{J}_\pm \equiv \hat{J}_x \pm i\hat{J}_y$ with no closed subsets. We will use the term "irrep" in this latter sense. Since the LMG Hamiltonian of Eq. (2) commutes with $\hat{J}^2$ [which is the Casimir element of $SU(2)$],

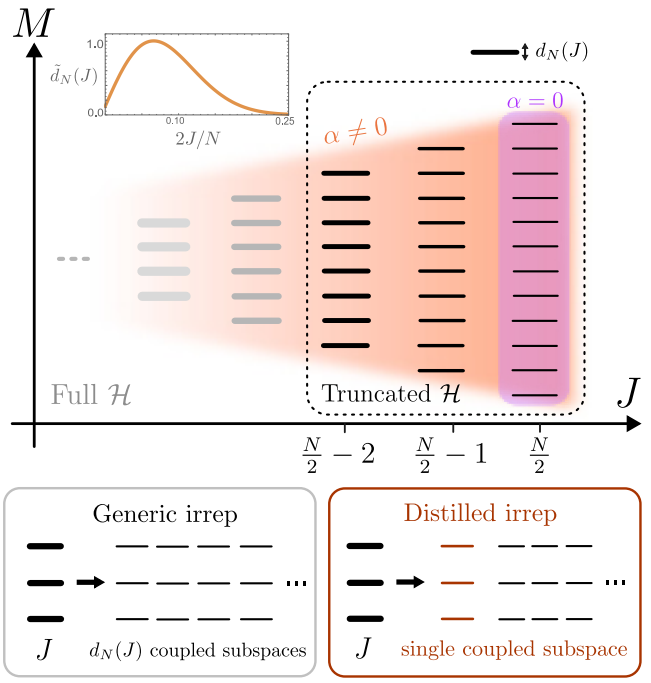


FIG. 2. (a) Schematic diagram of the Hilbert space structure for N spin-1/2 particles. States of definite $\hat{J}^2$ [eigenvalues $J(J+1)$] and $\hat{J}_z$ (eigenvalues M) are shown. Infinite-range interactions in Eq. (1), corresponding to $\alpha = 0$, can be described by states in the "irrep" with $J = N/2$, the symmetric subspace. When $\alpha \neq 0$, the symmetric subspace becomes coupled to lower-J subspaces, facilitating population-decay therefrom. The degeneracy of each irrep as a function of J of Eq. (8) is depicted in the inset plot normalized by its maximum value, i.e., $\tilde{d}_N(J) = d_N(J)/d_N^{\max}$, for $N = 100$. While lower irreps are degenerate, under a change of basis that respects (J,M), we can define nondegenerate "distilled" irreps that uniquely directly couple to the symmetric subspace.

its dynamics become closed within one such irrep determined by the initial state [29]. Formally, given N spin-1/2 particles, the Hilbert space decomposes as

$$\mathcal{H} = \mathcal{H}_{1/2}^{\otimes N} = \bigoplus_{J=(0,1/2)}^{N/2} \bigoplus_{u=1}^{d_N(J)} \mathcal{H}_{J,u}. \tag{7}$$

The tensor product of reducible representations contrasts with the direct-sum structure of irreps. Each irrep is specified by the quantum number of $\hat{J}^2$ (denoted J), and another quantum number u ranging from $u = 1$ to

$$d_N(J) = \frac{2J+1}{N/2+J+1}\binom{N}{N/2-J}. \tag{8}$$

Thus, there is a degenerate set of irreps with the same J. For general system size, the only nondegenerate irrep is when J takes its maximum value, $J = N/2$, known as the "symmetric subspace" as vectors in this irrep are symmetric under exchange of any two spin halves when viewed as a tensor product state. The combinatoric nature of the degeneracy factor shows exponential growth for $J \ll N/2$ (see inset in Fig. 2).

The standard basis of the irreps is the Dicke basis [30], the simultaneous eigenvectors of $\hat{J}^2$ and $\hat{J}_z$, augmented by

the degeneracy $|J, M, u\rangle$. Local degrees of freedom in the separable basis in Eq. (7), $\mathcal{H}_{1/2} = \text{span}(|\uparrow\rangle, |\downarrow\rangle)$, map onto qubits, $\{|\uparrow\rangle, |\downarrow\rangle\} \cong \{|0\rangle, |1\rangle\}$, and in the context of quantum computing, their tensor product is called the "computational basis." An arbitrary computational state is represented by $|\vec{s}\rangle \equiv |s_1\rangle \otimes |s_2\rangle \otimes \cdots |s_N\rangle$ for $s_j \in \{0, 1\}$.

The canonical change of basis from the Dicke basis to the computational basis is a recursive algorithm; there is no *closed-form* linear map between the two. The inner products $\langle\vec{s}|J, M, u\rangle$ come from the recursion relation of the Clebsch-Gordan series [29],

$$|J, M, u\rangle = C^{J,M}_{J-\frac{1}{2},M-\frac{1}{2};\frac{1}{2},\frac{1}{2}} |\uparrow\rangle \left|J - \tfrac{1}{2}, M - \tfrac{1}{2}\right\rangle + C^{J,M}_{J-\frac{1}{2},M+\frac{1}{2};\frac{1}{2},-\frac{1}{2}} |\downarrow\rangle \left|J - \tfrac{1}{2}, M + \tfrac{1}{2}\right\rangle, \quad (9)$$

$$|J, M, v\rangle = C^{J,M}_{J+\frac{1}{2},M-\frac{1}{2};\frac{1}{2},\frac{1}{2}} |\uparrow\rangle \left|J + \tfrac{1}{2}, M - \tfrac{1}{2}\right\rangle + C^{J,M}_{J+\frac{1}{2},M+\frac{1}{2};\frac{1}{2},-\frac{1}{2}} |\downarrow\rangle \left|J + \tfrac{1}{2}, M + \tfrac{1}{2}\right\rangle, \quad (10)$$

where $C^{J,M}_{j_1,m_1;j_2,m_2} = \langle J, M | j_1, m_1; j_2, m_2\rangle$ is a Clebsch-Gordan coefficient [31]. The procedure reveals that irrep degeneracy emerges from the choice of adding or subtracting subsystem angular momenta to construct total angular momentum. Beginning from a single degree of freedom $J = \frac{1}{2}$, the recursion proceeds by attaching another single spin, and using the Clebsch-Gordan series to split the levels into an additive $J + \frac{1}{2}$ and subtractive $J - \frac{1}{2}$ subspace. Attaching the next single spin, each subspace undergoes another round of level-splitting into additive and subtractive forms, etc. This recursive method becomes tedious and intractable as system size increases, especially for lower irreps $J \ll \frac{N}{2}$, where the degeneracy is most severe, although semiefficient analytic constructions of subsets of irreps have been formulated [32]. Moreover, since $|J, M, u\rangle$ behaves equivalently for all u under symmetric operations, the index u is arbitrary and its derivation from Clebsch-Gordan recursion is unnecessary for our purposes.

Instead, we seek a nonrecursive mapping between computational and Dicke states, beginning from the symmetric subspace. One can achieve a "top-down" change of basis transformation between the computational and irrep basis as follows. The symmetric subspace $\mathcal{H}_{N/2}$ is spanned by the Dicke States,

$$\left|\frac{N}{2}, M\right\rangle = \left\{|\uparrow\rangle^{\otimes \frac{N}{2}+M} |\downarrow\rangle^{\otimes \frac{N}{2}-M}\right\}_{\text{sym}}, \quad (11)$$

which are permutation-symmetric superpositions of $|\vec{s}\rangle$ with $\sum_j s_j = \frac{N}{2} - M$. More generally, one may define Dicke states from stretch states under the action of ladder operators,

$$|J, M, u\rangle = \frac{\hat{J}_-^{J-M} |J, J, u\rangle}{||\hat{J}_-^{J-M} |J, J, u\rangle||}, \quad (12)$$

directly from the definition of an irrep. The first irreps below the symmetric subspace, $\mathcal{H}_{N/2-1,u}$, are spanned by ladder operations [Eq. (12)] on each irrep's stretch state

$$\left|\frac{N}{2} - 1, \frac{N}{2} - 1, u\right\rangle = \sum_j c_j^{(1,u)} |\uparrow\rangle^{\otimes j-1} |\downarrow\rangle_j |\uparrow\rangle^{\otimes N-j}, \quad (13)$$

where $|\uparrow\rangle^{\otimes j-1} |\downarrow\rangle_j |\uparrow\rangle^{\otimes N-j}$ will be abbreviated $|\downarrow_j\rangle$, henceforth. Tautologically, $c_j^{(1,u)} \equiv \langle\downarrow_j | \frac{N}{2} - 1, \frac{N}{2} - 1, u\rangle$ are "computational amplitudes," but are nonunique whenever the first irreps are degenerated with multiple possible values of quantum number u. Similarly, within the second irreps $\mathcal{H}_{N/2-2,u}$, the stretch states are $|\frac{N}{2} - 2, \frac{N}{2} - 2, u\rangle = \sum_{j>k} c_{j,k}^{(2,u)} |\downarrow_j \downarrow_k\rangle$. Valid computational amplitudes must satisfy the following orthonormality relations:

$$\sum_j c_j^{(1,u)} = 0 = \sum_j c_{j,k}^{(2,u)}, \quad (14)$$

$$\sum_j c_j^{(1,u)} c_j^{(1,v)*} = \delta_{uv} = \frac{1}{2} \sum_{j,k} c_{j,k}^{(2,u)} c_{j,k}^{(2,v)*}, \quad (15)$$

$$c_{j,k}^{(2,u)} = c_{k,j}^{(2,u)}. \quad (16)$$

Equations (14)–(16) define the computational amplitudes. Stretched states of an irrep are annihilated by ladder operators $\hat{J}_+$ and the set of degeneracy indexed computational amplitudes form an orthonormal basis. Equation (16) follows from the commutativity of every spin-site degree of freedom with every other, since $\hat{\sigma}_z^{(j)} \hat{\sigma}_z^{(k)} = \hat{\sigma}_z^{(k)} \hat{\sigma}_z^{(j)}$. These constraints capaciously and specifically generate states with quantum numbers $J \in \{\frac{N}{2} - 1, \frac{N}{2} - 2\}$ and $M = J$, and so map onto the Dicke states obtained from Clebsch-Gordan recursion in Eqs. (9) and (10) via some unitary change of basis. We see then the freedom in defining the irreps within the degenerate manifolds. This freedom will be central to our method for "distilling" irreps to most efficiently approximate the dynamics of long-range interacting systems.

For time-independent symmetric all-to-all coupling models, such as the LMG, the Hamiltonian commutes with $\hat{J}^2$, and thus is block diagonal in the Dicke basis, with each irrep a closed block. A state initialized in the symmetric subspace will remain dynamically therein and restricted to an $N + 1$-dimensional Hilbert space, not 2^N dimensional. This block-closure of Hilbert space permits exact diagonalization of the LMG at general system sizes [33,34]. In contrast, the long-range Ising Hamiltonian generically couples all irreps dynamically. When the range exponent $\alpha > 0$, the collective spin symmetry is broken, and it has been shown that immediately the Hamiltonian becomes chaotic, and satisfies the ETH over the bulk of its spectrum [9]. For very long-range models, and for some parameters s, however, full ergodic exploration of the full exponentially large Hilbert space does not occur. In these cases, an $N + 1$-dimensional subset of eigenstates of $\hat{H}(s, \alpha)$ violates the ETH, which are the QMBS. The scar subspace $\mathcal{H}_{\text{QMBS}}$ maps to the symmetric subspace $\mathcal{H}_{J=N/2}$, such that $\lim_{\alpha\to 0} \mathcal{H}_{\text{QMBS}} = \mathcal{H}_{N/2}$. For this reason, initializing a system governed by $\hat{H}(s, \alpha)$ in a symmetric state $|\psi_0\rangle \in \mathcal{H}_{N/2}$ should result in dynamics dominated by the QMBS, and consequently remaining mostly within and close to the symmetric subspace. There are a small number of other eigenstates, away from the symmetric subspace that are more weakly nonthermal, and thus arguably form additional scars; we focus our attention on those eigenstates, which dress the symmetric subspace as they are the least disordered. We will test this hypothesis by constructing the general matrix elements of the transverse Ising Hamiltonian in the basis of Dicke states, up to the indeterminacy of irreps. We will then

truncate Hilbert space to keep only the states to which the symmetric subspace is directly coupled by the Hamiltonian's off-diagonal matrix elements and study range of validity of the resulting approximation.

C. Hamiltonian matrix elements

The permutation-asymmetric operator in $\hat{H}(s,\alpha)$ contains weight-2 interactions $\hat{\sigma}_z^{(j)}\hat{\sigma}_z^{(k)}$, and thus the Hamiltonian directly couples irreps differing by no more than 2 in total angular momenta,

$$\langle J', M'|\hat{H}(s,\alpha)|J, M\rangle \neq 0, \quad \text{only if} \quad |J - J'| \leqslant 2, \tag{17}$$

due to selection rules. This implies that to first order, the perturbed eigenstates will contain a small admixture of irreps $\mathcal{H}_{N/2-1,u}$ and $\mathcal{H}_{N/2-2,u}$, and no other subspaces couple to the symmetric subspace at this lowest order. These high J irreps are also the simplest to express, since they represent few-body excitations of otherwise symmetric collective states.

We seek a decomposition of $\hat{H}(s,\alpha)$ in the irrep basis of Dicke states. This requires an operator basis of irreducible operators to replace the *reducible* operator basis of Pauli products, $\hat{P}_{\alpha_1,\alpha_2,\ldots,\alpha_N} = \bigotimes_{i=1}^N \hat{\sigma}_{\alpha_i}$ (including $\hat{\sigma}_0 \equiv \mathbb{I}$). These operators in the basis we seek should also be covariant with other equal-weight operators under $SU(2)$ rotations, to guarantee Eq. (17). These criteria are satisfied by the generalized irreducible spherical tensor operators that map between irreps $\hat{T}_q^{(k)} : \mathcal{H}_{J',v} \to \mathcal{H}_{J,u}$, which obey the Wigner-Eckart theorem, and are defined in Refs. [35,36] as

$$\hat{T}_q^{(k)}[J, u; J', v] \equiv \sqrt{\frac{2k+1}{2J+1}} \sum_{M=-J'}^{J'} C_{J',M;k,q}^{J,M+q} \times |J, M+q, u\rangle\langle J', M, v|. \tag{18}$$

The generalized spherical tensor operators satisfy the requirements in Eq. (17),

$$\langle J', M'|\hat{T}_q^{(k)}|J, M\rangle \neq 0, \quad \text{only if} \quad |J - J'| \leqslant k, \tag{19}$$

due to Clebsch-Gordan selection rules. All tensor operators that map a given irrep to itself, $(J, u) = (J', v)$ are proportional to solid harmonics of angular momenta, projected onto that irrep,

$$\hat{T}_q^{(k)}[J, u; J, u] \propto \hat{\Pi}_{J,u}\mathcal{Y}_q^k(\hat{\mathbf{J}}), \tag{20}$$

where the projectors are $\hat{\Pi}_{J,u} \equiv \sum_M |J, M, u\rangle\langle J, M, u|$ and the solid harmonics are $\mathcal{Y}_q^{(k)}(r,\theta,\phi) \equiv \sqrt{\frac{4\pi}{2k+1}} r^k Y_q^{(k)}(\theta,\phi)$ derived from spherical harmonics $Y_q^{(k)}$. For example, restricting attention to a single irrep $\mathcal{H}_{J,u}$, the low-weight spherical tensors act on that irrep as follows [27]:

$$\hat{T}_0^{(0)} = \frac{\mathbb{I}}{\sqrt{2J+1}}, \tag{21}$$

$$\hat{T}_{-1}^{(1)} = \frac{\sqrt{3}\hat{J}_-}{\sqrt{2J(J+1)(2J+1)}}, \tag{22}$$

$$\hat{T}_0^{(1)} = \frac{\sqrt{3}\hat{J}_z}{\sqrt{J(J+1)(2J+1)}}, \tag{23}$$

$$\hat{T}_1^{(1)} = \frac{-\sqrt{3}\hat{J}_+}{\sqrt{2J(J+1)(2J+1)}}, \tag{24}$$

$$\hat{T}_{-2}^{(2)} = \frac{\sqrt{15}\hat{J}_-^2}{\sqrt{2J(J+1)(2J+1)(2J-1)(2J+3)}}, \tag{25}$$

$$\hat{T}_{-1}^{(2)} = \frac{\sqrt{15}(\hat{J}_z\hat{J}_- + \hat{J}_-\hat{J}_z)}{\sqrt{2J(J+1)(2J+1)(2J-1)(2J+3)}}, \tag{26}$$

$$\hat{T}_0^{(2)} = \frac{\sqrt{5}\left(4\hat{J}_z^2 - \hat{J}_+\hat{J}_- - \hat{J}_-\hat{J}_+\right)}{\sqrt{2J(J+1)(2J+1)(2J-1)(2J+3)}}, \tag{27}$$

$$\hat{T}_1^{(2)} = \frac{-\sqrt{15}(\hat{J}_z\hat{J}_+ + \hat{J}_+\hat{J}_z)}{\sqrt{2J(J+1)(2J+1)(2J-1)(2J+3)}}, \tag{28}$$

$$\hat{T}_2^{(2)} = \frac{\sqrt{15}\hat{J}_+^2}{\sqrt{2J(J+1)(2J+1)(2J-1)(2J+3)}}, \tag{29}$$

and so forth, for higher-weight tensors. Otherwise, when coupling two different irreps, spherical tensors cannot decompose into collective operators, but remain proportional to q-projected k-order products of Pauli operators. The generalized spherical tensors thus give a parsimonious representation of the Hamiltonian, as $\hat{H}(s,\alpha) \propto \hat{T}_q^{(k)}$ only for $k \leqslant 2$.

Pauli strings $\hat{P}_{\alpha_1,\alpha_2,\ldots,\alpha_N}$ and generalized spherical tensor operators $\hat{T}_q^{(k)}[J, u; J', v]$ both form complete orthonormal bases for operators on the N-qubit Hilbert space. The former is natural when considering local dynamics, where the latter is natural for considering nearly collective dynamics, especially when states occupy the symmetric subspace and topmost irreps. To express the Hamiltonian in the spherical tensor basis, note that $\hat{\sigma}_x^{(j)}$ is spanned by $\{\hat{T}_1^{(1)}[J, u; J', v],\ \hat{T}_{-1}^{(1)}[J, u; J', v]\}$, and $\hat{\sigma}_z^{(j)}\hat{\sigma}_z^{(k)}$ is spanned by $\{\hat{T}_0^{(0)}[J, u; J, v],\ \hat{T}_0^{(2)}[J, u; J', v]\}$. Furthermore, the uniform transverse field is permutation symmetric and thus does not couple different irreps, so we can express $\hat{H}(s,\alpha)$ in the spherical tensor basis as

$$\begin{aligned}\hat{H}(s,\alpha) = {} & s\sum_{J,u,v} F_0[\alpha, J, u, v]\hat{T}_0^{(0)}[J, u; J, v] \\ & + (s-1)\sum_{J,u} F_1[J] \\ & \times \left(\hat{T}_1^{(1)}[J, u; J, u] - \hat{T}_{-1}^{(1)}[J, u; J, u]\right) \\ & + s\sum_{J,u,v}\sum_{\delta_J=-2}^{2} F_2[\alpha, J, u; J+\delta_J, v] \\ & \times \hat{T}_0^{(2)}[J, u; J+\delta_J, v],\end{aligned} \tag{30}$$

a comparatively simple tensor structure, with no participation by $\hat{T}_q^{(k>2)}$. The scalar weights F_0, F_1, F_2 on each spherical tensor arise from their mutual trace with Pauli operators,

$$F_0[\alpha, J, u, v] = \frac{-1}{4\mathcal{N}}\sum_{j,k} |j-k|^{-\alpha} \times \mathrm{Tr}\left(\hat{\sigma}_z^{(j)}\hat{\sigma}_z^{(k)}\hat{T}_0^{(0)}[J, u; J, v]\right), \tag{31}$$

$$F_1[J] = \frac{1}{2}\sum_j \mathrm{Tr}\left(\hat{\sigma}_x^{(j)}\hat{T}_1^{(1)}[J, u; J, u]\right), \tag{32}$$

$$F_2[\alpha, J, u; J', v] = \frac{-1}{4\mathcal{N}}\sum_{j,k} |j-k|^{-\alpha} \times \mathrm{Tr}\left(\hat{\sigma}_z^{(j)}\hat{\sigma}_z^{(k)}\hat{T}_0^{(2)}[J, u; J', v]\right). \tag{33}$$

While F_1 affords closed-form solutions by simple Clebsch-Gordan rules, F_0 and F_2 are calculated by analyzing the Dicke-basis matrix elements $\langle J, M, u|\hat{\sigma}_z^{(j)}\hat{\sigma}_z^{(k)}|J', M, v\rangle$ in order to solve the mutual traces. The complete derivation is given in Appendix A. The most salient weights are those that couple $\mathcal{H}_{N/2}$ to $\mathcal{H}_{N/2-1,u}$ and $\mathcal{H}_{N/2-2,u}$,

$$F_2\left[\alpha, \frac{N}{2}, 0; \frac{N}{2}-1, u\right] = \frac{-1}{2\mathcal{N}}\sqrt{\frac{(N+2)(N+1)}{30(N-1)}} \times \sum_{j,k}\frac{c_j^{(1,u)} + c_k^{(1,u)}}{|j-k|^\alpha}, \tag{34}$$

$$F_2\left[\alpha, \frac{N}{2}, 0; \frac{N}{2}-2, u\right] = \frac{-1}{\mathcal{N}}\sqrt{\frac{N+1}{30}}\sum_{j,k}\frac{c_{jk}^{(2,u)}}{|j-k|^\alpha}, \tag{35}$$

which remain undefined until the computational amplitudes for each irrep are determined in accordance with the orthonormality rules Eqs. (14)–(16).

D. Irrep distillation

As discussed in Sec. II B, there is freedom in the choice of computational basis amplitudes due to the degeneracy of the irreps for $J < N/2$ within the constraints of Eqs. (14)–(16). This permits optimization of the sums $\sum_{j,k}|j-k|^{-\alpha}(c_j^{(1,u)} + c_k^{(1,u)})$ and $\sum_{j,k}|j-k|^{-\alpha}c_{j,k}^{(2,u)}$ in Eqs. (34) and (35), respectively. In particular, we can choose our irreps within the degenerate subspace to align most efficiently with the dynamic generated by the Hamiltonian. We achieve maximum magnitude in each of these sums with "bright" irreps, which maximally couple to the symmetric subspace via the Hamiltonian, in a method we call irreducible representation distillation (IRD). In fact, this coupling is kinematically exclusive; all other irreps are accessible from the symmetric subspace only by *multiple* actions of the Hamiltonian. Thus, irreducible representation distillation (IRD) solves the minimal dimension Hilbert space to first order perturbations beyond the symmetric subspace.

The interaction strength between two spins (j,k) in the system is determined by $|j-k|^{-\alpha}$, a complete undirected weighted graph taking spin sites as vertices, which imparts a concept of locality on the system by weighting interactions as a function of distance. Thus, hereafter, we refer to $|j-k|^{-\alpha}$ as a "localizing function." For the distilled irreps, the computational amplitudes are given by sums of the localizing function across one or more of its (symmetric) arguments: $\lambda_1^{(\alpha)}[j] \equiv \sum_{k=1}^N |j-k|^{-\alpha}$ and $\lambda_0^{(\alpha)} \equiv \sum_{j=1}^N\sum_{k=1}^{j-1}|j-k|^{-\alpha}$. From these sums, which marginalize the localizing function $|j-k|^{-\alpha}$ as shown in Fig. 3, the distilled computational amplitudes $\vec{c}^{(1,1)}$, $\vec{c}^{(2,1)}$ are then made to satisfy Eqs. (14)–(16) as

$$c_j^{(1,1)} = \frac{\lambda_1^{(\alpha)}[j] - \frac{2}{N}\lambda_0^{(\alpha)}}{\sqrt{\left(\sum_j \lambda_1^{(\alpha)2}[j]\right) - \frac{4}{N}\lambda_0^{(\alpha)2}}}, \tag{36}$$

$$c_{j,k}^{(2,1)} = \frac{(N-2)|j-k|^{-\alpha} - \lambda_1^{(\alpha)}[j] - \lambda_1^{(\alpha)}[k] + \frac{2}{N-1}\lambda_0^{(\alpha)}}{\sqrt{N-2}\sqrt{(N-2)\lambda_0^{(2\alpha)} + \frac{2}{N-1}\lambda_0^{(\alpha)2} - \sum_j \lambda_1^{(\alpha)2}[j]}}. \tag{37}$$

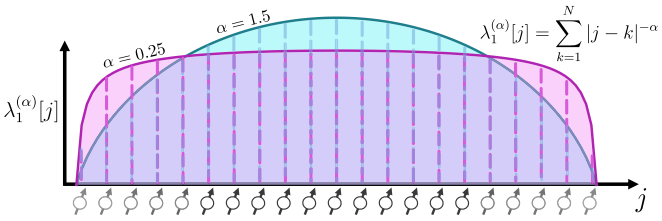


FIG. 3. Illustration of magnitudes of the amplitude on the $|\downarrow_j\rangle$ state of the distilled irrep corresponding to $J = N/2-1$ as in Eq. (13). Here, the "localizing function" weight $\lambda_1^{(\alpha)}[j]$ is proportional to $c_j^{(1,1)}$ in Eq. (36) up to norm and a constant offset. Shown are two values of α, for $\alpha = 0.25$ in magenta and $\alpha = 1.5$ in cyan. This choice of amplitudes ensures that the irrep constructed maximizes population transfer from the symmetric subspace for early timescales; hence, it is *distilled*.

It comes as no coincidence that distilled computational amplitudes take the form of orthonormalized marginals of the localizing function, because the sums in Eqs. (34) and (35) describe an inner product between the localizing function and the computational amplitudes in an $\binom{N}{1}$- or $\binom{N}{2}$-dimensional vector space. As a consequence of this maximum and the prior orthonormality relations,

$$\sum_j c_j^{(1,1)}c_j^{(1,u)*} = 0 \Rightarrow \sum_{j,k}\frac{c_j^{(1,u)} + c_k^{(1,u)}}{|j-k|^\alpha} = 0, \tag{38}$$

$$\sum_{j,k} c_{j,k}^{(2,1)}c_{j,k}^{(2,u)*} = 0 \Rightarrow \sum_{j,k}\frac{c_{j,k}^{(2,u)}}{|j-k|^\alpha} = 0, \tag{39}$$

meaning that to lowest order in perturbation theory, the Hamiltonian couples exactly three irreps to the symmetric subspace: the distilled irreps $\mathcal{H}_{N/2-1,1}$ and $\mathcal{H}_{N/2-2,1}$, and the symmetric subspace $\mathcal{H}_{N/2}$ itself. All nondistilled irreps with $J \geqslant \frac{N}{2}-2$, as well as all irreps with $J < \frac{N}{2}-2$, only affect dynamics at higher perturbative orders. We benefit from IRD by acquiring sufficient matrix elements to treat the QMBS as a first-order perturbation theory on LMG eigenstates. To this order, dynamics on exponential Hilbert space is restricted to the distilled subspace,

$$\mathcal{H}_D \equiv \mathcal{H}_{N/2} \oplus \mathcal{H}_{N/2-1,1} \oplus \mathcal{H}_{N/2-2,1}, \tag{40}$$

with $||\mathcal{H}_D|| = 3(N-1)$. This method of IRD generalizes to permutation symmetry-breaking functions beyond the algebraic decay function considered here, $|j-k|^{-\alpha}$, to any nonconstant coefficient with nonconstant marginals. Upon transforming into these distilled irreps and truncating Hilbert space down to $\mathcal{H}_D$, we obtain an approximation of the Hamiltonian $\hat{H}_D(s,\alpha) : \mathcal{H}_D \to \mathcal{H}_D$, whose properties we discuss below.

III. APPLICATIONS

A. Spectra and QMBS

Numerical comparisons between the distilled and exact systems are limited by the dimension of the exact Hamiltonian, which scales as 2^N. We losslessly compress this dimension by exploiting the aforementioned spin flip and mirror symmetries in the Hamiltonian to generate only the positive eigenstates of both symmetry operators when

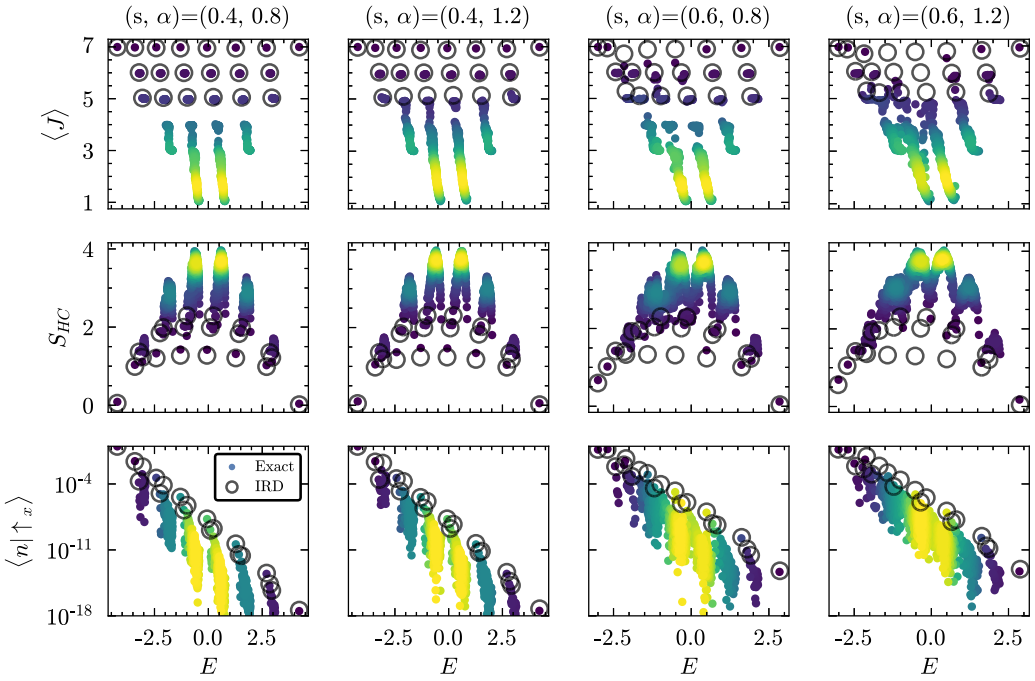


FIG. 4. Eigenstate properties of the exact Hamiltonian, $\hat{H}(s,\alpha)$, compared with the distilled and truncated Hamiltonian, $\hat{H}_D(s,\alpha)$. For eigenstates $|n\rangle$ (colored dots) and $|n_D\rangle$ (empty circles), plots in each row show spin number $\langle J\rangle$, half-chain entanglement entropy $S_{\rm HC}$, and overlap with X-polarized SCS, $|\langle n|J=\frac{N}{2},M_x=\frac{N}{2}\rangle|^2$. Two left-most columns with $s=0.4$ show full QMBS across eight eigenstates, two right-most columns with $s=0.6$ show broken QMBS. Dot color shows the density of data points due to irrep degeneracy, with yellow representing dense distributions.

diagonalizing. This slows, but does not eliminate the exponential scaling of Hilbert space.

Figure 4 introduces the quantum many-body scars of $\hat{H}(s,\alpha)$ by plotting some of these eigenstates' notable properties compared with the rest of the eigensystem. The QMBS in the long-range transverse Ising model are a set of $N+1$ eigenstates, spanning the spectrum with regular, smoothly varying energy separations [9], including the ground state and maximum energy states. Whereas most eigenstates have similar properties to those in their energy neighborhoods [6], the QMBS, as shown in Fig. 4, show much more symmetric properties than their energy neighbors. The QMBS are the eigenstates with high population in the symmetric subspace $\langle\hat{\Pi}_{N/2}\rangle > \frac{1}{2}$. Consequently, they take high spin numbers $\langle J\rangle \gtrsim \frac{N-1}{2}$, calculated as the expectation of $\sum_{J,u} J\langle\hat{\Pi}_{J,u}\rangle$, high overlap with spin-coherent states $|\langle n_{\rm QMBS}|\theta,\phi\rangle|^2 \gg 0$, and low entanglement entropy. The QMBS are the top $\langle J\rangle$ row of exact eigenstates in Figs. 4(a)–4(b), and for every scar state, there is a corresponding approximate scar state in the eigensystem of the distilled Hamiltonian $\hat{H}_D$. However, nonscar eigenstates of $\hat{H}_D$ (the second and third rows in $\langle J\rangle$) do not have high overlap with any exact eigenstates. Figure 4 demonstrates not only examples of the spectral form of the Hamiltonian at $N=14$, but also a few places where it is known to form QMBS, e.g., at $(s,\alpha)=(0.4, 0.8\sim 1.2)$, and where the QMBS is broken, such as at $(s,\alpha)=(0.6, 0.8\sim 1.2)$. A "broken" QMBS is one, which does not cover the full rank of the symmetric subspace. Instead, some eigenstates have significant population in both $\mathcal{H}_{N/2}$ and other irreps; these are the hybridized eigenstates and thus not scars. Previous work by Ref. [9] predicts broken scars wherever the coupling frequency between states within an irrep is resonant with the frequency between irreps. The close agreement of distilled eigenstates $|n_D\rangle$ to their exact counterparts $|n_{\rm QMBS}\rangle$ in terms of these observables indicates only that the approximation captures certain macroscopic properties and does not on its own clarify the approximation fidelity $|\langle n_D|n_{\rm QMBS}\rangle|^2$ nor the bounds on the QMBS regime.

Under distillation and truncation, the spectra of the resulting Hamiltonian successfully reproduce QMBS for all parameters, where QMBS appears in the exact Hamiltonian. Due to finite-size effects at small N, distillation also sometimes reconstructs false-QMBS even with parameters at which the exact Hamiltonian is not scarred. Insofar, as the QMBS consists of eigenstates whose dominant population is in $\mathcal{H}_{N/2}$, exhibiting spin numbers $\langle J\rangle \approx \frac{N}{2}$, couplings between the symmetric subspace and lower irreps is weak, justifying truncation. We proceed to measure ensemble-average properties over the ensemble of eigenstates with $\langle\Pi_{N/2}\rangle \geqslant \frac{1}{2}$, which are the candidates for QMBS. Under this logic, we expect that for a given scar state $|n_{\rm QMBS}\rangle$, there should be close tracking between $\langle J\rangle$ and IRD fidelity $\mathcal{F}\equiv|\langle n_{\rm QMBS}|n_D\rangle|^2$ despite there being no intrinsic connection between the two metrics. Consulting Fig. 5, we see exactly this tracking: The ensemble-average fidelity is high ($\overline{\mathcal{F}}\approx 1$) in Fig. 5(a) exactly where the ensemble-average spin number is near maximum ($\overline{\langle J\rangle}\approx\frac{N}{2}$) in Fig. 5(b). We see unit-average fidelities between distilled and exact scar states at every tractable system size, within well-defined parametric bounds. We will show in Sec. III B that these bounds grow stricter with increasing N, but are depicted at the finite size of $N=12$ in Fig. 5. There appears a broad region of strong QMBS for $s<0.6$ and all α, but with some slow decay with growing $\alpha>1$, and a liminal region

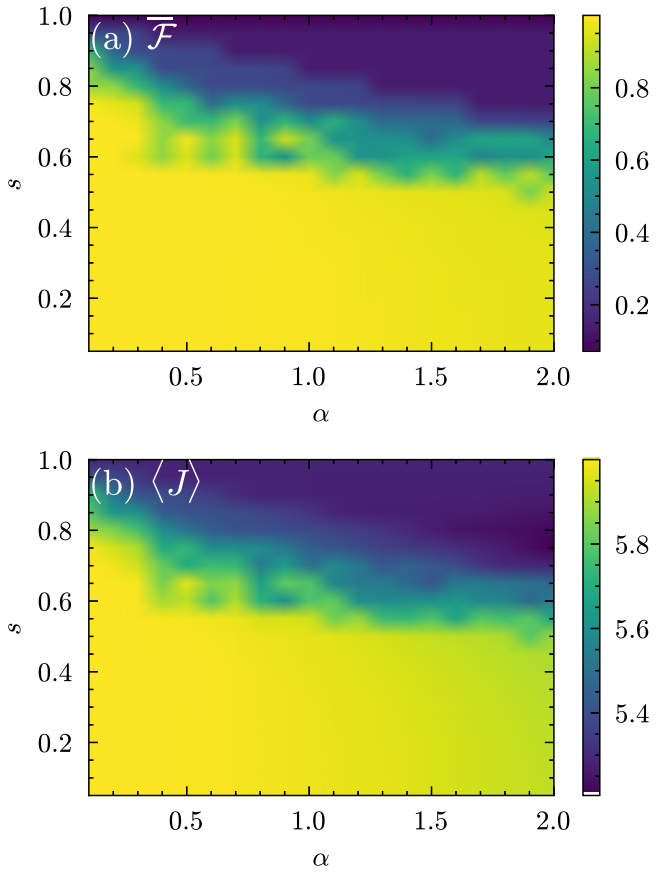


FIG. 5. Two different measures of the QMBS, for $N = 12$ across (s, α). (a) Average fidelity $\overline{\mathcal{F}}$ for $\mathcal{F} = |\langle n_{\text{QMBS}}|n_D\rangle|^2$ between the exact and distilled spectra. (b) Spin number $\overline{\langle J\rangle}$ over the same regime. The parameters in which the spectrum shows the strongest QMBS are also those in which distillation best captures these eigenstates, and this small system foreshadows the QMBS regime of larger systems: guaranteed scars for $s \lesssim 0.42$, though the small system is more forgiving of large α.

of QMBS for $0.6 < s < 0.8$ and $\alpha \ll 1$. In the large-system limit on a 1D spin chain, it is expected that $\frac{N}{2} - \langle J\rangle = \mathcal{O}(1)$ for $\alpha < \frac{1}{2}$, and $\frac{N}{2} - \langle J\rangle = \mathcal{O}(N^{2\alpha-1})$ for $\frac{1}{2} < \alpha < 1$ according to Ref. [9], guaranteeing a scalable approximation from IRD for very small α. For $\alpha \in (\frac{1}{2}, 1)$, scalable approximations require increasing orders of IRD, in the same fashion as the Lerose *et al.*'s rotor-magnon model [37] populates an increasing number of magnons. The more permissive preservation of QMBS at extremely long range, and slowly decaying QMBS as interaction ranges shrink, is precedented in the literature. Of more interest to us is the sharp boundary between QMBS and pure chaos brought about by small changes in s when the driving and interaction terms in the Hamiltonian are on the same scale. This suggests that the existence of QMBS as a function of s may follow a phase transition.

Breaches of the QMBS differ according to (s, α). At finite (though large) system size, shortening the range of interaction by increasing α gradually subverts scar states in the bulk of the spectrum due to strong coupling with lower irreps. Insufficient transverse driving (large s) allows spontaneous collapse of a few scar states due to strong hybridization with lower irrep states in the energy neighborhood, as explained in Ref. [9]. These degeneracies begin in the low-energy region of the spectrum near the ground state, and progress to higher energies as s grows beyond the critical point. The breach in the QMBS tracks with the unstable fixed point resulting from the classical energy function's bifurcation discussed in Sec. II A, which splits the single-well potential into two by raising the center, as associated with the GQPT. We hypothesize, therefore, that the instability seen in the classical phase space is associated with spontaneous violations of the QMBS. In the next section, we show how perturbation theory justifies the relationship between the quality of approximation by IRD and the existence of QMBS, by showing that the region of distillation self-consistency exactly matches the QMBS regime.

B. Bounds on QMBS

Upon truncating to the distilled irreps, the remaining Hilbert space is $3(N-1)$-dimensional, far smaller than the full 2^N-dimensional Hilbert space, and reproduces the QMBS up to first-order perturbative expansions in energy eigenstates. Consider a perturbation theory where the zeroth order is the LMG Hamiltonian from Eq. (2) and the perturbation is $\hat{V}(s, \alpha)$. The eigenstates in the symmetric subspace, $|n_{\text{sym}}\rangle$, are those obeying Eqs. (4) and (5) with $\hat{J}^2|n_{\text{sym}}\rangle = \frac{N}{2}(\frac{N}{2}+1)|n_{\text{sym}}\rangle$ and thus $|n_{\text{sym}}\rangle \in \mathcal{H}_{N/2}$. The perturbed eigenenergies and eigenstates in this subspace are

$$E'_n = E_n + \langle n_{\text{sym}}|\hat{V}(\alpha)|n_{\text{sym}}\rangle, \tag{41}$$

$$|n'\rangle = |n_{\text{sym}}\rangle + \sum_{m\neq n} \frac{\langle m|\hat{V}(\alpha)|n_{\text{sym}}\rangle}{E_n - E_m}|m\rangle, \tag{42}$$

where $|m\rangle$ runs over *all* eigenstates of $\hat{H}(s, 0)$ in every irrep, not only those in the symmetric subspace. Whether one defines the perturbation $\hat{V}(\alpha) \equiv \hat{H}(s, \alpha) - \hat{H}(s, 0)$ or $\hat{V}(\alpha) \equiv \hat{H}_D(s, \alpha) - \hat{H}_D(s, 0)$, where $\hat{H}_D$ is the irrep-distilled, truncated Hamiltonian, the first-order perturbed eigensystem in Eqs. (41) and (42) is unchanged. This is because the above truncation does not affect any matrix elements mapping to or from $\mathcal{H}_{N/2}$. Furthermore, because the QMBS are the eigenstates of $\hat{H}(s, \alpha)$, which are "dressed" symmetric eigenstates, a perturbation theory of the dressed symmetric eigenstates is also one of the QMBS.

The degree to which the perturbed eigenstates are not eigenstates of the exact Hamiltonian can be quantified by their energy uncertainty with respect the desired Hamiltonian,

$$\Delta E_{n'} \equiv \sqrt{\langle n'|\hat{H}_D^2|n'\rangle - \langle n'|\hat{H}_D|n'\rangle^2}. \tag{43}$$

This uncertainty forms the leading-order correction to eigenstate evolution, and consequently dictates the rate of short-time decay in dynamical fidelity, such as Loschmidt echoes (to be described in Sec. III D). The growth of energy variance, especially of its ensemble average $\overline{\Delta E} \equiv \sum_{n'} \frac{\Delta E_{n'}}{N+1}$, and ensemble maximum $\Delta E_{\max} \equiv \max_{n'} \Delta E_{n'}$, predict worst-case performance of the convergence of perturbation theory, and consequently of the QMBS itself. We use $\Delta E_{\max}$ as a self-consistency test of IRD at large system size.

Figure 6 depicts the growth of energy variance in the perturbed eigenstates as (s, α) increase. The sharp increase in

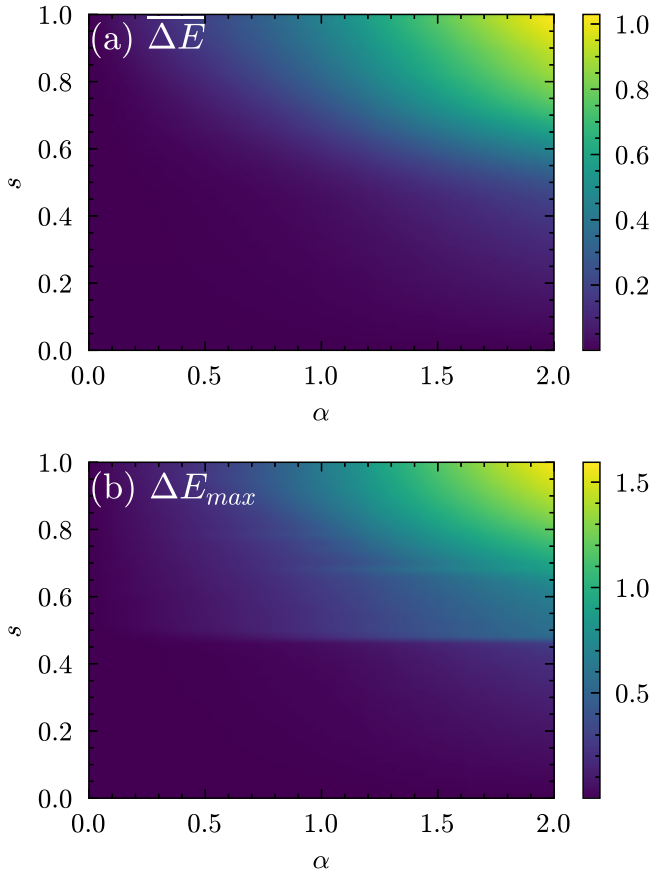


FIG. 6. Energy uncertainty ΔE, defined in Eq. (43), as a measure of the accuracy of the distilled eigenstates for $N = 100$, across (s, α). (a) Scar-average variance $\overline{\Delta E}$. (b) Scar-maximum variance $\Delta E_{\max}$. All energy variances remain small when $s < 0.5$ at this system size. The maximum $\Delta E_{\max}$ shows a sharp jump at $s = 0.5$.

$\Delta E_{\max}$ at $s = 0.5$ in Fig. 6(b) coincides with the emergence of an unstable fixed point in $E(s; \theta, \phi)$ from Eq. (6), which gives rise to the GQPT. Finite-size scaling analysis (FSSA) shows the placement of this discontinuity at $s = 0.5$ is a finite-size effect, and in the thermodynamic limit, the critical point is $s_c \approx 0.42$, as we find in Appendix B. By contrast, Fig. 6(a) is smooth, $\overline{\Delta E}$ is insensitive to the critical point. Let us emphasize this point, that $\Delta E_{\max}$ witnesses the phase transition but $\overline{\Delta E}$ does not, indicates that the breakdown in the QMBS must start locally, affecting one or a few eigenstates. In any case, when ΔE reaches a significant fraction of the inter-scar level spacing, then perturbation theory and IRD no longer agree or converge, and the dynamical fidelity (measured by Loschmidt echoes) of the nonconvergent scar state decays rapidly. In the regime of $\alpha < \frac{1}{2}$, all ΔE remain small for all s, reproducing the bounds of absolute QMBS stability predicted by Ref. [9]. A similar, though more gradual boundary at $\alpha = 1$ (also observed in Loschmidt echoes) limits the long-range regime to the lattice dimension, and this boundary likewise correlates with the preservation or decay of dynamical fidelity.

Notably, the bounds on IRD self-consistency indicated by Fig. 6 align with the parameters where QMBS is known to exist at finite system size, attested by Fig. 5. Thus, not only can IRD capture the spectral and state properties of QMBS within the QMBS regime, it can test its own self-consistency without recourse to the full-dimensional system, and is self-consistent wherever there exists an unbroken QMBS.

C. Quantum phase transitions

Having demonstrated that IRD truncation well approximates the QMBS, we now consider whether distillation preserves order parameters in long-range interacting spin Hamiltonians *outside* the QMBS regime, such as QPTs. The GQPT and DQPT defined in Sec. II A, both are defined by an order parameter given by the system polarization $\langle J_z \rangle$. Since $\langle J_z \rangle$ is a "macro" observable, two dynamical systems whose microstates severely differ may still agree on that macrostate [26]. Here, we render expectation scale invariant to system size by defining $\mathbf{X} \equiv \frac{2}{N}\langle \mathbf{J} \rangle$, and of these, we consider the QPTs in terms of $Z = \frac{2}{N}\langle J_z \rangle$. In both QPTs, for small s, the system exhibits paramagnetic alignment of the spins with the transverse field; for large s, the system enters an increasingly ferromagnetic phase as each spin aligns with its neighbors along the longitudinal axis. These two phase transitions differ in their critical values of s, and whether their origins are kinematic or dynamic.

The GQPT is defined by the Hamiltonian's ground state $|n = 0\rangle$ (which generically lies on the corner of the tower of states, and thus safely within the QMBS) with critical $s_{\text{GQPT}} = \frac{1}{2}$ in the case of the LMG, shown in Fig. 7(a) in blue. The GQPT's ferromagnetic phase results from twofold degeneracy in the ground state at infinite system size, corresponding to the aforementioned pitchfork bifurcation in the classical energy function $E(s; \theta, \phi)$. In the paramagnetic phase, the ground state is spin-flip symmetric, but superpositions of the degenerate ground states in the ferromagnetic phase can spontaneously break this symmetry, resulting in $\overline{\langle J_z \rangle}_{\text{GQPT}} = \langle n = 0 | \hat{J}_z | n = 0 \rangle \neq 0$ wherein the overline signifies an infinite time average, which is trivial for expectation values of Hamiltonian eigenstates. This is the case in the classical limit; at finite system size, there is always an energy gap between the true ground state (a symmetric superposition of the bottom of each well) and the first excited state (an antisymmetric superposition). However, this energy gap shrinks exponentially with system size, even below the numerical precision of computational eigensolvers; when the gap is smaller than the floating-point resolution, eigensolvers break the symmetry, which we exploit to find nonzero Z in the near-ground manifold. Likewise at finite size, the GQPT is not visible at $s = \frac{1}{2}$ itself, due to Heisenberg uncertainty and ensuing finite width of the ground-state's wave function covering shallow double-well potentials. Instead, the GQPT becomes measurable only at $s^{(N)}_{\text{GQPT}} > \frac{1}{2}$, where the double-well energy function becomes deep enough to distinguish the two "degenerate" ground states; more accurately, $\lim_{N\to\infty} s^{(N)}_{\text{GQPT}} = \frac{1}{2}$.

Meanwhile, the DQPT is defined by quench dynamics starting in the Z-polarized state, $|J = \frac{N}{2}, M = \frac{N}{2}\rangle$ and measuring the infinite time average $\overline{\langle J_z \rangle}_{\text{DQPT}} = \lim_{T\to\infty} \frac{1}{T}\int_0^T \langle \hat{J}_z \rangle(t) dt$. As discussed in Sec. II A, the DQPT's paramagnetic phase occurs when the initial collection spin direction lies outside the separatrix, and dynamics restore the initial state's spontaneously broken spin-flip symmetry.

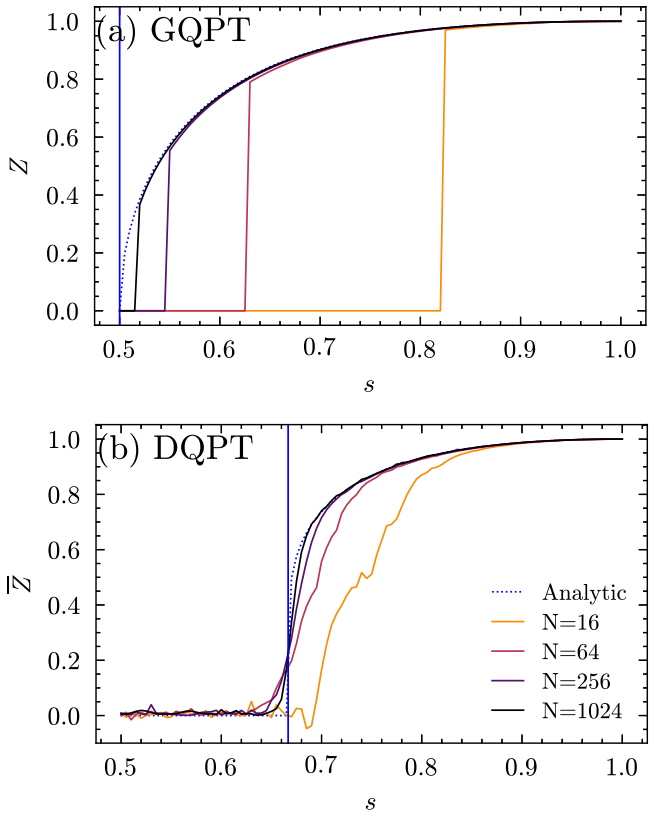


FIG. 7. The QPTs within $s \in [0.5, 1]$ for $\alpha = 1$ at various N. (a) The GQPT measured by Z. (b) The DQPT measured by $\overline{Z}$ with an integraion time of $T = 10^5$. In both cases, as system size increases, the curves approach the analytic thermodynamic limits (blue dotted lines).

On the other hand, in the ferromagnetic phase, the initial state is inside the separatrix and bound to one of the two wells, whereupon the spontaneously broken symmetry is not dynamically restored. The critical point is calculated by setting $E(s_{\mathrm{DQPT}}; 0, 0) = E(s_{\mathrm{DQPT}}; \frac{\pi}{2}, 0)$ and solving for s_{DQPT}. For the LMG model, the critical point occurs at $s_{\mathrm{DQPT}} = 2/3$, shown in Fig. 7(b) in blue. Previous work by Žunkovič *et al.* [20] has found that s_{DQPT} remains well defined with order parameter $\overline{Z}$ for $\alpha \leqslant 2$, but using time-dependent variational principle (TDVP) evolution at smaller system sizes with coarser numerics. We will pursue larger systems and longer times with finer combs of s. In any case, for all finite N, both s_{GQPT} and s_{DQPT} are outside the QMBS regime determined in Sec. III B, so we cannot expect IRD to well approximate the microstate evolution, rather, we must test the order parameter evolution separately.

The GQPT in Fig. 7(a) and DQPT in Fig. 7(b), are both faithfully represented by distilled irreps, and they approach the analytic forms in the thermodynamic limit, taken from Ref. [38]. Figure 7 shows these QPTs for system sizes $N \in \{16, 64, 256, 1024\}$, wherein growing system sizes approach $s^{(N)}_{\mathrm{GQPT}} \to \frac{1}{2}$ and $s^{(N)}_{\mathrm{DQPT}} \to \frac{2}{3}$ as expected. Moreover the derivative $\frac{d}{ds}\overline{Z}$ becomes smooth at large N, and sharply increases around the critical point. Although not shown in Fig. 7, the distilled QPTs' behavior are largely constant across α for a given N, thanks to Kac normalization.

That the GQPT cleaves so tightly to its limit behavior under the LMG is well explained by the spectrum; the ground state of $\hat{H}(s, \alpha)$ remains extremely close to, or exactly within, $\mathcal{H}_{N/2}$ across nearly all parameters. This is because both operator components, the transverse field and longitudinal interaction, have their expectation values extremized by symmetric states. Thus, the ground state (and, sometimes, the maximally excited state) are both well represented under distillation even when the QMBS is otherwise comprehensively broken. However, the DQPT has no such spectral alibi, and so illustrates a recurring point appearing across the field of many-body physics, that certain classes of macrostatic observables remain robust even in chaotic systems that should be resistant to approximation, and even under highly reductive and seemingly unstable approximation schemes.

Both of the QPTs are explained by the classical energy $E(s; \theta, \phi)$, which lives in the phase-space representation of the symmetric subspace $\mathcal{H}_{N/2}$. That the DQPT and GQPT remain largely unchanged under distillation and truncation at finite α suggests not only that the distilled Hilbert space abides by a kind of phase space, but that the energy landscape of said phase space changes only perturbatively in the long-range interaction regime, from its collective limit. But of course, the distilled subspace is not closed under long-range dynamics, and so in addition to energy functions, we must consider the stability of states in phase space.

D. Dynamics of nonclassical states

The IRD allows for the models of dynamics beyond mean field-classical approximation. Two canonical examples of nonclassical states, squeezed and cat states, are both generated by the Ising and LMG family of Hamiltonians. Because dynamical instability and chaos cause slightly perturbed points in phase space to diverge in their evolution, these regimes can efficiently split classical wave functions into quantum superpositions. Beyond the pitchfork bifurcation for $s > s_{\mathrm{GQPT}}$, the unstable fixed point at $(\theta, \phi) = (\frac{\pi}{2}, 0)$ or at $|\uparrow_x\rangle$ propels that initialization along the separatrix, squeezing, and then splitting it into a cat state [22]. Since at $s = s_{\mathrm{DQPT}}$, said separatrix passes through the Z poles, then $\hat{H}(\frac{2}{3}, 0)$ acting on $|\theta = \frac{\pi}{2}, \phi = 0\rangle$ can generate a Z-polarized spin-GHZ state: $\frac{1}{\sqrt{2}}(|\frac{N}{2}, \frac{N}{2}\rangle + |\frac{N}{2}, -\frac{N}{2}\rangle)$.

But instability and chaos, which are useful for rapid state development, also combine into ergodic decay of coherences. For all $s \in (0, 1)$ and all $\alpha > 0$, then $\hat{H}(s, \alpha)$ is generically chaotic; but only at $s \geqslant \frac{1}{2}$ does it gain an unstable phase space in its symmetric manifold. To illustrate the implication of the GQPT in the breakdown of the QMBS and ensuing failure of approximation, we turn to Loschmidt analysis. For two Hamiltonians $\hat{H} \approx \hat{H}'$ and an initial state $|\psi\rangle$, the Loschmidt echo is defined,

$$\mathcal{M}(\psi, t) \equiv |\langle\psi| e^{i\hat{H}'t} e^{-i\hat{H}t} |\psi\rangle|^2. \tag{44}$$

The timescale and initialization subspace over which $\mathcal{M} \approx 1$ determines the conditions under which $\hat{H}'$ can dynamically reproduce the fine-grained structure of $\hat{H}$.

Consider $\hat{H} = \hat{H}_D(s, \alpha)$, the distilled Hamiltonian, $\hat{U}_{\mathrm{QMBS}}(t) \equiv \sum_{n'} e^{-iE'_{n'}t} |n'\rangle\langle n'| \approx e^{-i\hat{H}'t}$, the time-evolution map spanned by the perturbed scar states constructed in

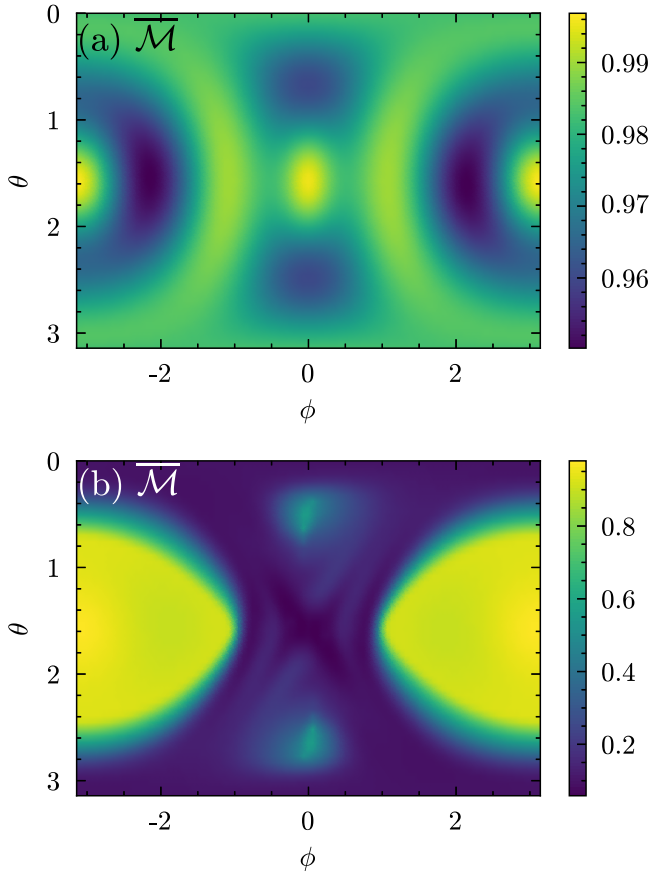


FIG. 8. Time-averaged SCS Loschmidt echoes $\overline{\mathcal{M}}(\theta, \phi)$, from Eq. (45), for $N = 100$, $\alpha = 0.4$, and a total averaging time $T = 20$ as a function of the direction of an initial spin coherent state $|\theta, \phi\rangle$. (a) Within the QMBS regime at $s = 0.4$, all initial polarizations maintain high fidelity over short evolutions. (b) At the DQPT critical point $s = s_{\mathrm{DQPT}}$, initializations near the separatrix and unstable fixed point fail to converge in approximate evolution.

Eqs. (41) and (42), which approximates a unitary over that subspace, and an initial SCS, $|\theta, \phi\rangle$. We can approximately decompose $|\theta, \phi\rangle \approx \sum_{n'} \langle n'|\theta, \phi\rangle |n'\rangle$, and accordingly define

$$\mathcal{M}(\theta, \phi; t) = |\langle \theta, \phi | \hat{U}^{\dagger}_{\mathrm{QMBS}}(t) e^{-i\hat{H}_D(s,\alpha)t} |\theta, \phi\rangle|^2$$

$$= \left| \sum_{n'} \langle \theta, \phi | n' \rangle e^{iE'_{n'}t} \langle n' | e^{-i\hat{H}_D t} |\theta, \phi\rangle \right|^2 \quad (45)$$

$$\approx |\langle \theta, \phi | e^{i\hat{H}'t} e^{-i\hat{H}_D(s,\alpha)t} |\theta, \phi\rangle|^2. \quad (46)$$

Note that all the population of $|\theta, \phi\rangle$ outside the span of the perturbed scars is projected away, by $\hat{U}_{\mathrm{QMBS}}$ that acts only on a subspace, suppressing the Loschmidt echo. As discussed in Sec. III B, for $t \ll \frac{1}{\Delta E}$, $\mathcal{M}(n', t) \approx 1 - (\Delta E_{n'} t)^2$. That is, the energy variance forms the leading order term in Loschmidt echo decay. We time-average the Loschmidt echo as $\overline{\mathcal{M}}(\theta, \phi)$, and plot the results in Fig. 8.

Figure 8 demonstrates the impact of the boundary shown in Fig. 6 on dynamical fidelity across the Bloch sphere. Figure 8(a) shows $\overline{\mathcal{M}}(\theta, \phi)$ for parameters with uniformly low ΔE, indicating all trajectories in the symmetric subspace are well approximated over considerable time. But Fig. 8(b) shows that at $s = s_{\mathrm{DQPT}}$, the unstable fixed point and the separatrix crossing over it have $\overline{\mathcal{M}} \approx 0$, indicating rapid decay. The two wells above and below the unstable fixed point, and especially the high-energy region on either side, have far stronger echoes. In fact, the high-energy region suggests remaining scars that do not fully cover the symmetric subspace. This and other corroborating findings imply that the breach in the QMBS, and consequently the nonconvergence of IRD's approximation along specific trajectories, results from the combination of chaos from long-range interactions and instabilities in the collective phase space beyond the GQPT. These results extend those from Ref. [9] and confirm their prediction of QMBS hybridization around excited-state QPT energy bands at large system size.

The discrepancy between the critical value associated with the breakdown in QMBS ($s_c \approx 0.42$) and the point of ground-state quantum phase transition ($s_{\mathrm{GQPT}} = 0.5$) can be understood as follows. Recall that the GQPT is a phase transition in a macroscopic parameter, which is insensitive to fine-grained structure, which would first be detected by spectral quantities like $\Delta E'_n$. Moreover, the phase space of the long-range system, even in the thermodynamic limit, is higher dimensional than a simple sphere for 1 degree of freedom, and unstable trajectories may emerge in the full phase space, whose instability not seen in (θ, ϕ).

Unstable trajectories in phase space permit rapid evolution to generate nonclassical states, but in chaotic systems, they also breach the QMBS. Since IRD approximates the QMBS, it cannot accurately represent dynamics along these trajectories, although it still captures stable regions of phase space even in parametric regimes that include these unstable fixed points and separatrices. Moreover, irrep distillation can perfectly well represent nonclassical states, even if stable IRD dynamics can only generate them slowly. Consulting Fig. 9, states that reside mostly within the symmetric subspace, but that do not resemble spin-coherent states, commonly emerge from dynamics in the QMBS regime, visible in the shrinking R^2 net polarization. Likewise, the effects of long-range QMBS dynamics on prior-prepared nonclassical states, like the GHZ state in red, may come of interest, so the ability of IRD to predict these dynamics presents utility.

IV. DISCUSSION

A. Comparison with other methods

Irrep distillation is not the only approximate method for representing long-range interacting spin ensembles in their near-collective scenarios. Three others are established in literature: time-dependent spin-wave theory [37,39] and its refinement in the rotor-magnon model [9], matrix product states (MPS) [19,40], and discrete truncated Wigner approximation (DTWA) [24,41]. Compared with these formalisms, IRD has a clear use case in the construction and dynamics of highly nonlocal/entangled collective states on generic lattice geometries, with guaranteed dynamical fidelity.

Time-dependent spin-wave theory is highly scalable, as it combines the Holstein-Primakoff and Gaussian approximations, but it inherits their modeling limitations. It cannot represent, let alone evolve, nonpolarized or non-Gaussian-like

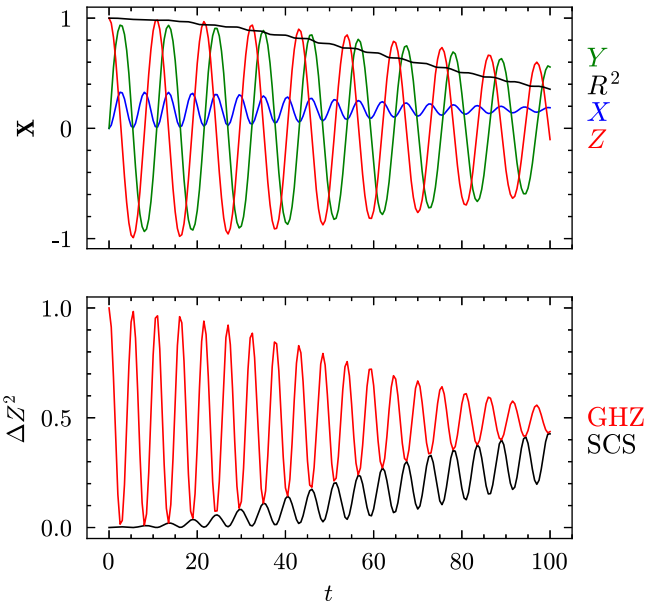


FIG. 9. Dimensionless collective observable of distilled evolution, $\mathbf{X}$, at $N = 400$, $(s, \alpha) = (0.4, 0.8)$, initialized in Z-polarized states. Top: X, Y, Z, and $R^2 \equiv ||\mathbf{X}||^2$ (black). Bottom: $\Delta Z^2 \equiv \frac{4}{N^2}(\langle J_z^2\rangle - \langle J_z\rangle^2)$ initialized in SCS (black), and GHZ (red).

states such as spin-GHZ states, despite such states residing purely in the symmetric subspace. Irrep distillation retains the symmetric subspace as a Hilbert space, allowing it to both represent and sometimes generate weakly- and nonpolarized collective states, as discussed in Sec. III D. Recent work by Lerose *et al.* [9] extends the spin-wave formalism for long-range spin models into a "rotor-magnon" picture, by retaining the standing-wave mode as a collective spin degree of freedom, and performing the Holstein-Primakoff transformation on all other modes. This affords their formalism access to generic Dicke states, albeit in an overcomplete nonorthogonal basis that demands periodic boundary conditions. Irrep distillation benefits modestly from periodic boundaries but accommodates open boundaries and other inhomogeneous lattice geometries perfectly well, as shown above.

That same work outlines a "shell" truncation [9], of which, IRD is a more efficient refinement; an δ-shell truncation restricts Hilbert space to all the irreps with $J \geqslant \frac{N}{2} - \delta$, including degeneracies; this incurs a truncated dimension $||\mathcal{H}^{(\delta)}_{\text{shell}}|| = \mathcal{O}(\frac{N^{\delta+1}}{\delta!})$, against which IRD provides a polynomial speedup while sacrificing very little fidelity. This is because many of the irreps in each "shell" are very weakly coupled to the others, and so we consolidate or discard them.

MPS methods are useful tensor-network computational tools for efficient solutions of ground states (density matrix renormalization group, or DMRG) and time evolution for both short-range and long-range [42] interactions (time-dependent variational principle, or TDVP). MPS evolution is most efficient when entanglements are short range and shallow, with a built-in time limit as entanglement generically grows over dynamics. But all MPS methods inherit the lattice-geometric limitation baked into its left/right-operator notation, so it struggles with most systems on multidimensional lattices, where entanglement is too thoroughgoing to truncate. Irrep distillation is agnostic to lattice geometry, whether a chain, an irregular graph, a cubic grid, triangular couplings, etc. The lattice geometry and dimension is encoded in the relative strengths of couplings between sites, so in two and three dimensions, our method generically outperforms MPS.

DTWA represents an initial state exactly as a discrete Wigner function, then evolves it according to the Poisson bracket (rather than the Moyal bracket), as though under a classical Hamiltonian. While DTWA is as efficient as the construction of its initialization, and seems to reproduce correct order parameters in a variety of systems [24], it is an uncontrolled approximation. DTWA is not guaranteed to converge and only justified heuristically postfacto, and so requires independent verification. Irrep distillation's grounding in perturbation theory and its connection to QMBS provides it with guarantees and internal checks via self-consistency metrics (e.g., energy variances ΔE and Loschmidt echoes $\mathcal{M}$).

B. Two-body model

IRD provides a way of understanding the dynamics of long-range interacting systems in terms of minimal decomposition into subsystems and degrees of freedom. Recall that the infinite-range Hamiltonian is exactly represented by a one-body collective spin model with 1 degree of freedom, while the finite-range system is properly many bodies. Here, we show that IRD allows us to interpret the dynamics as a few-body model, specifically with 2 degrees of freedom to first order in perturbation theory. Furthermore, this interpretation reintroduces a tensor-product decomposition of degrees of freedom, with the mathematical benefit of well-defined entanglement. A standard quantification of entanglement in many-body systems is the entanglement entropy from a half-chain partition, but whenever this entropy saturates due to volume-law entanglement, it becomes intractable to calculate at large N. The entropy following from our tensor-product decomposition saturates according to an area law, and we show that the low entanglement generated dynamically in the few-body picture arises from the optimality of the decomposition.

The distilled, truncated Hilbert space of irreps $\mathcal{H}_D \equiv \bigoplus_{\delta=0}^{2} \mathcal{H}_{N/2-\delta}$ defined in Eq. (40) has dimension $||\mathcal{H}_D|| = 3(N-1)$, and by inspection, maps exactly onto a two-body Hilbert space $\mathcal{H}_D = \mathcal{H}_1 \otimes \mathcal{H}_{N/2-1}$ via the Clebsch-Gordan series, analogous to Eqs. (9) and (10) and shown diagrammatically in Fig. 10. That is, for all $|m, M\rangle \equiv |1, m\rangle \otimes |\frac{N}{2} - 1, M\rangle$ such that $|1, m\rangle \in \mathcal{H}_1$ and $|\frac{N}{2} - 1, M\rangle \in \mathcal{H}_{N/2-1}$, then

$$\left|\frac{N}{2} - \delta, M\right\rangle = \sum_{m=-1}^{1} C^{N/2-\delta,M}_{N/2-1,M-m;1,m} |m, M-m\rangle, \tag{47}$$

$$|m, M\rangle = \sum_{\delta=0}^{2} C^{N/2-\delta,M+m}_{N/2-1,M;1,m} \left|\frac{N}{2} - \delta, M+m\right\rangle, \tag{48}$$

which appropriately has Hilbert dimensions $||\mathcal{H}_1|| = 3$ and $||\mathcal{H}_{N/2-1}|| = N-1$. As Fig. 10 shows, through this mapping from a trio of subspaces onto a pair of subsystems (the "major" spin $|\frac{N}{2} - 1, M\rangle$ and "minor" spin $|1, m\rangle$), we can interpret the effect of IRD as partitioning the N spin-half

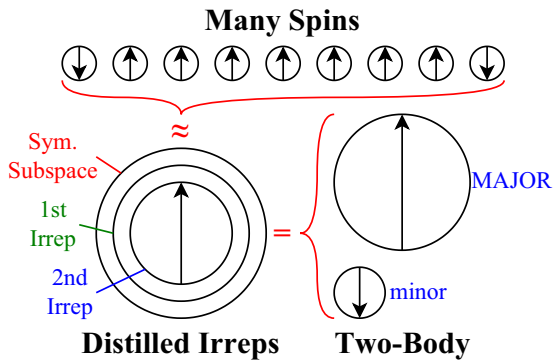


FIG. 10. An ensemble of identical half-spin particles, represented in the collective-spin basis, may have its state truncated into a nondegenerate set of distilled irreps. These distilled irreps then form the exact collective-spin basis of a pair of particles, which each encompass nonlocal degrees of freedom from the many-body ensemble.

particles into a set of $N-2$ and a set of 2. This partition groups together the sets of maximum coöperation so that the $N-2$ spin halves are approximately represented by a single spin-$\frac{N}{2}-1$ major particle, while the remaining two spin halves are approximated by a spin-1 minor particle. The major and minor particles are nonlocal degrees of freedom, in contrast to the local spin-degrees of freedom in the computational basis. Whereas each subsystem $\mathcal{H}_{1/2}^{(j)} \subset \mathcal{H}_{1/2}^{\otimes N}$ encodes the full information accessible by measurements on the spin at the jth site and only that spin, the minor particle corresponds superpositionally to the information in all spins. The major and minor particles are nonlocal degrees of freedom, in the same way as wave number degrees of freedom under Fourier transforms, or parity/phase degrees of freedom in the Bell basis.

By the same token, the lowest order of permutation asymmetry and noncollective behavior is reflected in asymmetries between the major and minor particle states, visible in their entanglement. Considering the two-body basis and tracing over either the major or minor particle, $\hat{\rho}_M = \mathrm{Tr}_m(\hat{\rho})$, $\hat{\rho}_m = \mathrm{Tr}_M(\hat{\rho})$ we achieve an alternative (generically lesser) entanglement entropy,

$$S_{TB} = -\mathrm{Tr}(\hat{\rho}_M \ln \hat{\rho}_M) = -\mathrm{Tr}(\hat{\rho}_m \ln \hat{\rho}_m). \tag{49}$$

We compare this to the entanglement entropies calculated by tracing over any two *local* degrees of freedom in the exact system. For spin sites $j, k \in [1, N]$ and density matrix $\hat{\rho} : \mathcal{H}_{1/2}^{\otimes N} \to \mathcal{H}_{1/2}^{\otimes N}$,

$$\hat{\rho}_{\neg j,k} \equiv \mathrm{Tr}_{j,k}(\hat{\rho}), \quad S_{\neg j,k} = -\mathrm{Tr}(\hat{\rho}_{\neg j,k} \ln \hat{\rho}_{\neg j,k}), \tag{50}$$

in which there are $\binom{N}{2}$ unique values of (j, k). Thus, we define maximum, mean, and minimum entropies across the ensemble of computational-basis partial traces,

$$S_{\max} = \max_{j,k} S_{\neg j,k}, \tag{51}$$

$$\overline{S} = \frac{2}{N(N-1)} \sum_{j,k} S_{\neg j,k}, \tag{52}$$

$$S_{\min} = \min_{j,k} S_{\neg j,k}, \tag{53}$$

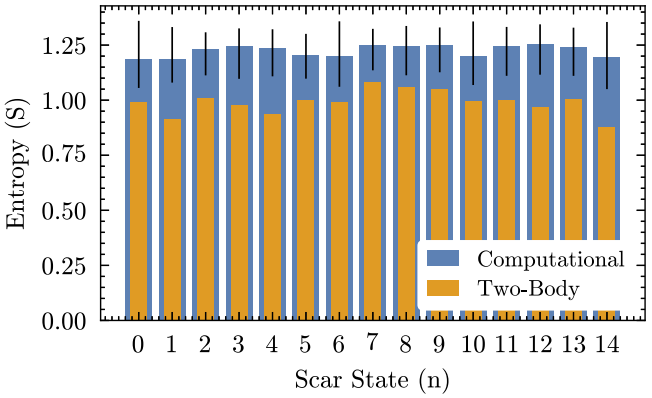


FIG. 11. Entanglement entropies from partial traces over $N-2$: 2 partitions, for each eigenstate $|n\rangle$ in the QMBS of a 14-spin system. Computational entropies show the range and mean of $S_{j,k}$ (blue with bounds). Two-body entropy S_{TB} shown inside, always less than every computational entropy for the same state.

and measure these entropies and S_{TB} for the QMBS of the distilled Hamiltonian.

Figure 11 shows this comparison of entropies, demonstrating that across the QMBS, $S_{\mathrm{TB}} \leqslant S_{\min}$, suggesting that the two-body mapping effectively selects the partition $N-2:2$ across which there is the *least* entanglement, optimizing over both local and nonlocal degrees of freedom. The optimization over nonlocal degrees of freedom is paramount; were the two-body model constrained to assign two specific sites (j, k) to fall under the purview of $\mathcal{H}_1$, then the two-body entropy would be bound below $S_{\mathrm{TB}} = S_{\min}$. By the monogamy of entanglement, consequently the minor and major particles each encloses the most collectively coöperating (ergo entangled) degrees of freedom.

Discrepancies between S_{TB} and $S_{\min}$ arise from two sources, primarily that the two-body mapping isolates and localizes correlations, which are scrambled in the computational basis, thereby presenting an infimum (but not necessarily minimum) for entanglement from all possible $N-2:2$ partitions. Because partial traces over the computational basis only respect local degrees of freedom, if the greatest correlations are nonlocal, then no choice of (j, k) minimizes the entropy. The two-body model is constructed from the first-order expansion of the symmetric subspace $\mathcal{H}_{N/2}$ under the Hamiltonian $\hat{H}(s, \alpha)$. This means the first coherences in symmetric initial states to break down dynamically are those between the major and minor particle, and so this subsystem decomposition generates the least entanglement under $\hat{H}(s, \alpha)$ out of any basis. In the limit case of the LMG at $\alpha = 0$, the system restores permutation symmetry, and $(S_{\max} = \overline{S} = S_{\min} = S_{\mathrm{TB}})|_{\alpha=0}$, as is expected when all $N-2:2$ partitions, whether local or nonlocal, are equivalent. Secondarily, disagreement may be systematic between the distilled $\hat{H}_D$ and the exact $\hat{H}$, as when outside the QMBS regime. In this case, $S_{\mathrm{TB}} \not\leqslant S_{\min}$ because perturbation theory is nonconvergent and the distillation-approximate QMBS is a poor approximation.

V. CONCLUSION AND OUTLOOK

In this investigation, we have defined an approach to study quantum many-body systems with long-range

interactions that truncates the exponentially large Hilbert space in a manner that efficiently captures the desired dynamics. Our scheme is motivated by QMBSs, which yield ordered dynamics on nonintegrable many-body spin systems analogous to their integrable collective counterparts, and we isolate the QMBS by a special truncation of Hilbert space. This truncation, via IRD exploits irrep degeneracy to solve for "bright" irreps that dress the collective system, thereby reproducing the first-order perturbation theory of the QMBS with minimal matrix elements. We deployed IRD on the long-range interacting transverse field Ising Hamiltonian, since its infinite-range limit is the integrable LMG. Using Loschmidt echoes on the perturbation-theoretic QMBS, we tested the self-consistency of IRD, finding a clear set of parametric bounds wherein the perturbed scars are all near eigenstates under distilled dynamics. We related these bounds to the existence and collapse of the QMBS itself, as a product of unstable trajectories in the classical phase space resulting from the GQPT, extending previous theories of QMBS breakdown [9]. Even outside these parametric bounds, we found that distilled dynamics reproduce the QPTs of the LMG, corroborating prior results [20].

The bounds on the applicability of IRD is closely related to the existence of unstable fixed points in the classical limit, and the range of interactions. We find that critical coupling strength $s \leqslant s_c^{(N)}$ for $\lim_{N\to\infty} s_c^{(N)} = 0.42$ (approaching the limit from above) and $\alpha < 1$, agree with the bounds $\alpha < d$ given by Ref. [9] for lattice dimension d. In addition, the form of the breakdown in QMBS at $s > s_c$ fulfills that paper's prediction, that approximate energy degeneracies between states of neighboring spin-number levels would lead to hybridization in the corresponding eigenstates, and consequent breakdown of the level separation. The correspondence of this QMBS collapse with the GQPT critical point extends to the individual hybridizing eigenstates, being those with population along the phase-space separatrix. The position of the energy region wherein this degeneracy arises varies smoothly with $s \in [0.5, 1]$ at $0 < \alpha \ll 1$, vindicating the prior spectral description of such breakdowns occurring because of resonances in two smoothly varying characteristic frequencies of the Hamiltonian. Moreover, the authors of Ref. [9] speculated from small-N spectra the generic breaking of scar states along the saddle points and separatrices of QPTs, which we have observed through perturbative Loschmidt analysis at large N.

The method of IRD, and its interpretation as a reduction to a few spin degrees of freedom, is agnostic of lattice geometry, and remains mathematically well defined for any Hamiltonian with a finite number of permutation symmetry-breaking terms, regardless of the support of those operators or the forms of accompanying symmetric terms. If couplings between the symmetric subspace and lower subspaces can be attributed to a finite number of low-weight operators modulated by localizing functions, then IRD can optimize a set of nondegenerate or low-fold degenerate irreps, which exclusively couple via said localizing functions. Furthermore, IRD is a controlled approximation thanks to its correspondence with perturbation theory, and for any finite N, a sufficiently high order of IRD (described below) will converge to the full Krylov subspace of the QMBS. Its region of applicability is efficiently testable. Finally, IRD can represent and even slowly generate nonpolarized, nonclassical, non-Gaussian states because it retains the mathematical structure of a (truncated) Hilbert space. This combination of features makes IRD somewhat unique among the other approximations in Sec. IV A, and these differences have profound implications for simulation.

To illustrate this, consider the application of IRD to control the many-body state in the symmetric subspace, but with finite-range interaction. Such control has been of great interest recently for applications to metrology, with the production of spin-squeezed states in arrays of Rydberg atoms in optical tweezers [43,44]. A $2 \sim 3$D lattice of atoms described by a spin XX model will exhibit QMBS with a strong overlap with the symmetric subspace and large energy gap. Through application of a time-dependent driving field, the system is in principle "controllable," meaning that one can implement any unitary map within the symmetric subspace. To achieve this, one can employ quantum optimal control, but this requires the ability to efficiently integrate the time-dependent Schrödinger equation. IRD provides the formalism necessary to do so. MPS would struggle to solve the dynamics of even modest two-dimensional lattices. Time-dependent spin waves could not represent non-Gaussian target states. DTWA would not permit fine-grained analysis of which subspaces afford high-fidelity simulation under highly nonclassical dynamics. We will explore this application in future work.

The IRD method presented here corresponds to only a first-order perturbation theory; one can conceive of higher orders of IRD, which acquire the minimal matrix elements for corresponding orders of perturbation theory. Tentative results suggest that any finite-order IRD will truncate to a linear Hilbert dimension $||\mathcal{H}_D|| = \mathcal{O}(N)$, but with a prefactor that increases exponentially with the perturbative order. For example, while we have shown that first-order IRD gives $||\mathcal{H}_D^{(1)}|| = 3(N-1)$, we have reason to believe that second-order IRD $\mathcal{H}_D^{(2)}$ includes *only* low-fold degenerate irreps with $J \geqslant \frac{N}{2} - 4$. Similarly, permutation-symmetric operators are generically difficult experimentally, so Hamiltonians that include multiple weakly permutation-asymmetric components merit their own treatment under distillation. These extensions, along with proofs of their hierarchy of couplings and generalized few-body interpretations is the subject of forthcoming research.

Finally, the first-order approximation of a many-body Hamiltonian from a one-body ansatz is a few-body model (in this case, two bodies) inviting an interpretation of dynamics through a semicollective lens, such as the extension of QPTs directly from the few-body phase space. The LMG's quantum phase transitions emerge as a consequence of bifurcations and separatrices in its classical energy function. These critical points are also visible in the quantum phase-spatial analog, the Weyl symbol $W_{\mathrm{LMG}}(\theta, \phi)$. Extensions of Weyl symbols to multiple irreps are provided by Klimov and Romero [35,36], but cannot accommodate irrep degeneracy. By distilling and truncating, we can derive approximate Weyl symbols for the long-range Hamiltonian, both in the irrep basis and by mapping onto a doubled phase space $(\Theta, \Phi; \theta, \phi)$ corresponding to the two-body model. These Weyl symbols may reproduce the critical behavior, which explains the preservation of quantum phase transitions into the long-range regime, or may reveal new phase transitions, which are irreducibly multibody.

ACKNOWLEDGMENTS

We thank Anupam Mitra for helpful discussions. We acknowledge funding from the U.S. National Science Foundation, with Grant No. PHY-2210013. This material is based upon work supported by the Air Force Office of Scientific Research, under Awards No. FA9550-22-1-0498 and FA9550-20-1-0123.

DATA AVAILABILITY

The data that support the findings of this article are not publicly available. The data are available from the authors upon reasonable request.

APPENDIX A: DERIVATION OF HAMILTONIAN TENSOR WEIGHTS

Here, we provide a more structured method for analytically solving F_0, F_1, F_2 as they appear in Eq. (30). First and easiest, we see by examination that Eq. (32) simplifies to

$$F_1[J] = \mathrm{Tr}\big(\hat{J}_x \hat{T}_1^{(1)}[J,u;J,u]\big), \tag{A1}$$

and further simplification comes from constraining Eq. (18) to demand $(J,u) = (J',v)$, for which the low-ordered Clebsch-Gordan coefficient provides a simple closed-form expression: $C^{J,M+1}_{J,M;1,1} = \sqrt{\frac{(J-M)(J+M+1)}{2J(J+1)}}$, which is clearly proportional to the matrix elements of $\hat{J}_+$. A mechanical calculation along these lines quickly reveals that

$$F_1[J] = \sqrt{\frac{J(J+1)(2J+1)}{6}}. \tag{A2}$$

Such closed forms will prove unavailable for the general cases F_0 and F_2, however.

Canonically, the traces in Eqs. (31) and (33) are solved via the Clebsch-Gordan series of angular momentum addition, outlined in Eqs. (9) and (10). This is intractable at larger system sizes, representing a bottom-up approach to acquire collective states from smaller spin ensembles. If we concern ourselves only with the symmetric subspace and other large irreps, we need a top-down analytic expression for F_0 and F_2. Toward this end, we solve

$$\mathrm{Tr}\big(\hat{\sigma}_z^{(j)}\hat{\sigma}_z^{(k)}\hat{T}_0^{(0)}[J,u;J,v]\big) = \sum_M \langle J,M|\hat{\sigma}_z^{(j)}\hat{\sigma}_z^{(k)}|J,M\rangle\langle J,M|\hat{T}_0^{(0)}|J,M\rangle, \tag{A3}$$

$$\mathrm{Tr}\big(\hat{\sigma}_z^{(j)}\hat{\sigma}_z^{(k)}\hat{T}_0^{(2)}[J,u;J',v]\big) = \sum_M \langle J',M|\hat{\sigma}_z^{(j)}\hat{\sigma}_z^{(k)}|J,M\rangle\langle J,M|\hat{T}_0^{(2)}|J',M\rangle, \tag{A4}$$

wherein the matrix elements of $\hat{T}_q^{(k)}$ can be specified by placing constraints on Eq. (18), while those of $\hat{\sigma}_z \otimes \hat{\sigma}_z$ we proceed to solve here.

The aforementioned matrix elements in Dicke space are given for $J' \leqslant J \leqslant J'+2$ as

$$\langle J,M|\hat{\sigma}_z^{(j)}\hat{\sigma}_z^{(k)}|J',M\rangle = \frac{\langle J,J'|\hat{J}_+^{J'-M}\hat{\sigma}_z^{(j)}\hat{\sigma}_z^{(k)}\hat{J}_-^{J'-M}|J',J'\rangle}{||\langle J,J'|\hat{J}_+^{J'-M}||\cdot||\hat{J}_-^{J'-M}|J',J'\rangle||}, \tag{A5}$$

since up to vector norm, general Dicke states are equivalent to the stretch states of their irreps, under the action of lowering operators. We simplify the above by taking a normal-order operator form so the ladder operators act on the bra, and the Paulis act on the stretch-state ket. We use $SU(2)$ commutation relations to acquire this normal ordering, and the recursion relation of ladder operators to renormalize the Dicke states,

$$\hat{J}_+^n\hat{\sigma}_z^{(j)}\hat{\sigma}_z^{(k)}\hat{J}_-^n = \hat{J}_+^n\hat{J}_-^n\hat{\sigma}_z^{(j)}\hat{\sigma}_z^{(k)} - 2n\hat{J}_+^n\hat{J}_-^{n-1}\big(\hat{\sigma}_z^{(j)}\hat{\sigma}_-^{(k)} + \hat{\sigma}_-^{(j)}\hat{\sigma}_z^{(k)}\big) + 4n(n-1)\hat{J}_+^n\hat{J}_-^{n-2}\hat{\sigma}_-^{(j)}\hat{\sigma}_-^{(k)}, \tag{A6}$$

$$||\hat{J}_-^n|J,M\rangle|| = \sqrt{\frac{(J-M+n)!(J+M)!}{(J-M)!(J+M-n)!}}. \tag{A7}$$

Application of these identities yields the general expression for Dicke-space matrix elements of dual Pauli matrices,

$$\langle J,M|\hat{\sigma}_z^{(j)}\hat{\sigma}_z^{(k)}|J',M\rangle = \sqrt{\frac{(J-M)!(J'+M)!(J+J')!}{(J'-M)!(J+M)!(2J')!(J-J')!}}\Bigg(\sum_{\vec{s}}(-1)^{s_j+s_k}\langle J,J'|\vec{s}\rangle\langle\vec{s}|J',J'\rangle - \frac{2(J'-M)}{\sqrt{(J+J')(J-J'+1)}}\sum_{\vec{s}}\langle J,J'|\vec{s}\rangle((-1)^{s_j}s_k\langle\vec{s}\oplus 1_k|J',J'\rangle + (-1)^{s_k}s_j\langle\vec{s}\oplus 1_j|J',J'\rangle) + \frac{4(J'-M)(J'-M-1)}{\sqrt{(J+J')(J+J'-1)(J-J'+2)(J-J'+1)}}\sum_{\vec{s}}s_js_k\langle J,J'|\vec{s}\rangle\langle\vec{s}\oplus(1_j,1_k)|J',J'\rangle\Bigg), \tag{A8}$$

for computational basis states $|\vec{s}\rangle$ for $\vec{s}\in\mathbb{B}^{\otimes N} \cong \{0,1\}^{\otimes N} \cong \{\uparrow,\downarrow\}^{\otimes N}$. In Eq. (A8), we have an expression for Pauli operators in the irrep basis, which is nearly closed form, but for the ambiguity of the inner products between Dicke and computational states, $\langle J,J'|\vec{s}\rangle$. By closing this final ambiguity, it will become possible to analytically express Dicke-basis matrix elements of the Hamiltonian within the largest irreps, without recourse to lower irreps or recursion relations.

Consider for example $\mathcal{H}_{N/2}$, $\mathcal{H}_{N/2-1,u}$ and $\mathcal{H}_{N/2-2,u}$, since only those subspaces are directly coupled to the symmetric subspace at lowest order. In these cases, we can relate $\langle J,J'|\vec{s}\rangle$ to computational amplitudes defined in Eqs. (14)–(16), as such:

$$\left\langle \frac{N}{2},\frac{N}{2}\right| \uparrow\Big\rangle^{\otimes N} = 1, \tag{A9}$$

$$\left\langle \frac{N}{2}, \frac{N}{2}-1 \middle| \downarrow_j \right\rangle = \frac{1}{\sqrt{N}}, \tag{A10}$$

$$\left\langle \frac{N}{2}, \frac{N}{2}-2 \middle| \downarrow_j\downarrow_k \right\rangle = \sqrt{\frac{2}{N(N-1)}}, \tag{A11}$$

$$\left\langle \frac{N}{2}-1, \frac{N}{2}-1, u \middle| \downarrow_j \right\rangle = c_j^{(1,u)}, \tag{A12}$$

$$\left\langle \frac{N}{2}-1, \frac{N}{2}-2, u \middle| \downarrow_j\downarrow_k \right\rangle = \frac{c_j^{(1,u)}+c_k^{(1,u)}}{\sqrt{N-2}}, \tag{A13}$$

$$\left\langle \frac{N}{2}-2, \frac{N}{2}-2, u \middle| \downarrow_j\downarrow_k \right\rangle = c_{j,k}^{(2,u)}, \tag{A14}$$

and so forth.

Substituting appropriate computational amplitudes for the inner products $\langle J, J'|\vec{s}\rangle$ in Eq. (A8), then performing the mutual traces in Eqs. (A3) and (A4), and summing over the localizing function as in Eqs. (31) and (33) gives closed-form expressions for the unknown matrix weights, within the concerned subspaces

$$F_0\left[\alpha, \frac{N}{2}, 0, 0\right] = \frac{\sqrt{N+1}}{12}(1-N), \tag{A15}$$

$$F_0\left[\alpha, \frac{N}{2}-1, u, v\right] = \frac{\sqrt{N-1}}{12}\left((1-N)\delta_{uv} + \sum_{j,k}\frac{2}{\mathcal{N}|j-k|^\alpha}\left(c_j^{(1,u)}-c_k^{(1,u)}\right)^* \times \left(c_j^{(1,v)}-c_k^{(1,v)}\right)\right), \tag{A16}$$

$$F_0\left[\alpha, \frac{N}{2}-2, u, v\right] = \frac{\sqrt{N-3}}{12}\left((1-N)\delta_{uv} - \sum_{j,k}\frac{2}{\mathcal{N}|j-k|^\alpha}\left(\sum_m \left(c_{jm}^{(2,u)}+c_{km}^{(2,u)}\right)^*\left(c_{jm}^{(2,v)}+c_{km}^{(2,v)}\right) + 2c_{jk}^{(2,u)*}c_{jk}^{(2,u)} - 2\sum_m\left(c_{jm}^{(2,u)*}c_{jm}^{(2,v)}+c_{km}^{(2,u)*}c_{km}^{(2,v)}\right)\right)\right), \tag{A17}$$

$$F_2\left[\alpha, \frac{N}{2}, 0; \frac{N}{2}, 0\right] = \frac{-1}{6}\sqrt{\frac{(N+3)(N+2)(N+1)(N-1)}{5N}}, \tag{A18}$$

$$F_2\left[\alpha, \frac{N}{2}, 0; \frac{N}{2}-1, u\right] = \frac{-1}{2\mathcal{N}}\sqrt{\frac{(N+2)(N+1)}{30(N-1)}}\sum_{j,k}\frac{c_j^{(1,u)}+c_k^{(1,u)}}{|j-k|^\alpha}, \tag{A19}$$

$$F_2\left[\alpha, \frac{N}{2}, 0; \frac{N}{2}-2, u\right] = \frac{-1}{\mathcal{N}}\sqrt{\frac{N+1}{30}}\sum_{j,k}\frac{c_{jk}^{(2,u)}}{|j-k|^\alpha}, \tag{A20}$$

$$F_2\left[\alpha, \frac{N}{2}-1, u; \frac{N}{2}-1, v\right] = \frac{1}{6}\sqrt{\frac{(N+1)N(N-1)}{5(N-2)(N-3)}}\left((1-N)\delta_{uv} + \sum_{j,k}\frac{1}{\mathcal{N}|j-k|^\alpha}\left(2\left(c_j^{(1,u)*}c_j^{(1,v)}+c_k^{(1,u)*}c_k^{(1,v)}\right)+c_j^{(1,u)*}c_k^{(1,v)}+c_k^{(1,u)*}c_j^{(1,v)}\right)\right), \tag{A21}$$

$$F_2\left[\alpha, \frac{N}{2}-1, u; \frac{N}{2}-2, v\right] = \frac{1}{2\mathcal{N}}\sqrt{\frac{N(N-1)}{30(N-4)}}\sum_{j,k}\frac{1}{|j-k|^\alpha}\left(2\left(c_j^{(1,u)*}+c_k^{(1,u)*}\right)c_{jk}^{(2,v)} - \sum_m c_m^{(1,u)*}\left(c_{jm}^{(2,v)}+c_{km}^{(2,v)}\right)\right), \tag{A22}$$

$$F_2\left[\alpha, \frac{N}{2}-2, u; \frac{N}{2}-2, v\right] = \frac{1}{6}\sqrt{\frac{(N-1)(N-2)(N-3)}{5(N-4)(N-5)}}\left((1-N)\delta_{uv} - \sum_{j,k}\frac{1}{\mathcal{N}|j-k|^\alpha}\left(4c_{jk}^{(2,u)*}c_{jk}^{(2,v)} - \sum_m\left(\left(c_{jm}^{(2,u)}+c_{km}^{(2,u)}\right)^*\times\left(c_{jm}^{(2,v)}+c_{km}^{(2,v)}\right)+\left(c_{jm}^{(2,u)*}c_{jm}^{(2,v)}+c_{km}^{(2,u)*}c_{km}^{(2,v)}\right)\right)\right)\right). \tag{A23}$$

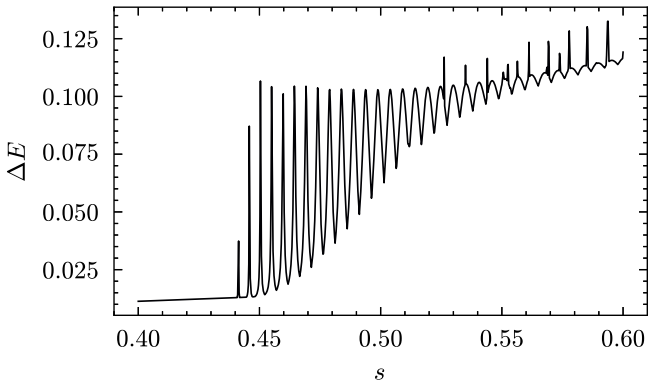


FIG. 12. The maximum energy variance of distilled eigenstates, $\Delta E_{\max}$, for $N = 128$ and $\alpha = 0.5$, plotted over $s \in [0.4, 0.6]$. At low s, a stable region shows uniformly low ΔE, followed by a series of oscillations with sharp peaks and smoothly increasing troughs, beginning well below the apparent border of $s = 0.5$ depicted in the coarse-grained Fig. 6(b).

Of these, Eqs. (A19) and (A20) are reproduced in the main text as Eqs. (34) and (35), motivating the move to irreducible representation distillation.

APPENDIX B: FINITE-SIZE SCALING ANALYSIS

Coarse-grained measurements of $\Delta E_{\max}$ according to Eq. (43) and Fig. 6 find a sharp increase in the worst-case

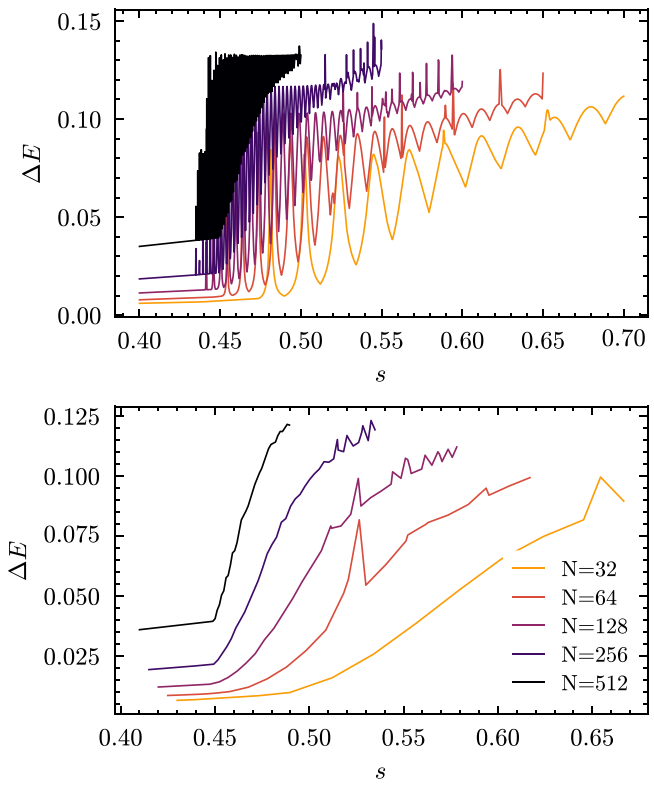


FIG. 13. Maximum energy variance $\Delta E_{\max}$, for $\alpha = 0.5$ and $N \in \{32, 64, 128, 256, 512\}$, plotted over small ranges in s. Top: full scans in s, showing sharp oscillations. Bottom: local minima selected from above, showing mostly smooth increase of ΔE.

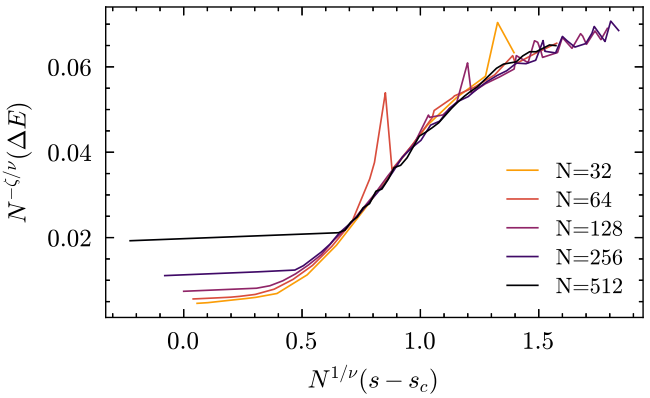


FIG. 14. The maximum energy uncertainty of distilled eigenstates, $\Delta E_{\max}$, for $\alpha = 0.5$, plotted across s. Local minima in s show smooth increase of $\Delta E_{\max}$. Manually scaled $N^{-\zeta/\nu}\Delta E_{\max}$ against $N^{1/\nu}(s - s_c)$ finding $s_c \approx 0.42$, $\nu \approx 2$, and $\zeta \approx 0.2$. At all observed system sizes, QMBS breakdown occurs beyond $s > 0.44$, after the critical point.

approximation of Hamiltonian eigenstates by perturbation theory, at a specific point in s. Here, we determine the form of this increase in $\Delta E_{\max}$ with s via fine-grained numerics around the apparent critical point, and use manual FSSA to approximate the this critical point and associated critical exponents. The result is an apparent phase transition in the convergence of perturbation theory with s in association with (but distinct from) the GQPT described in the main text. Figure 12 shows a plot of $\Delta E_{\max}$ against a small parameter range of $s \in [0.4, 0.6]$, corresponding to a cross section of Fig. 6 at $\alpha = 0.5$ and $N = 128$, with greater data resolution. At this scale, it becomes clear that the sharp jump in $\Delta E_{\max}$ at $s \approx 0.5$ shown in Fig. 6(b) is not the only nonsmooth point: In fact, $\Delta E_{\max}$ depends sensitively on small changes in s to determine the relative frequencies in $\hat{H}(s, \alpha)$ and therefore the quality of perturbation theory. This means that within a small neighborhood of $s \in [s' - \delta s, s' + \delta s]$, there are exceptionally lucky and unlucky values of s, which quicken or delay the convergence of perturbative expansions to the Hamiltonian eigensystem, as combing across s hybridize and dehybridize different scar states according to spectral resonances [9]. However, we also see from Fig. 12 that best-case values of $\Delta E_{\max}$ (i.e., local minima) seem to grow smoothly as s increases across the displayed range, implying that all perturbation theories within the neighborhood $s' \pm \delta s$ will uniformly worsen as the center of that neighborhood, s', crosses some critical value s_c.

The apparent point of transition from low to high $\Delta E_{\max}$ depends on N, however, as shown in Fig. 13, likewise the oscillations become sharper as system size increases. Figure 12(a) finds that the bounds on low $\Delta E_{\max}$ shift to lower values of s at large system size, indicating that the QMBS regime becomes stricter in the thermodynamic limit. As the oscillations are not a finite-size effect, but endemic to the relationship between $\Delta E_{\max}$ and s at all scales, it is necessary to find a smooth subset of the data to use for FSSA [shown in Fig. 13(b)], which are the local minima selected from the full dataset in Fig. 13(a), and curated to exclude oscillatory regimes outside the transition of interest.

To find the critical point of this phase transition, we employ FSSA, which assumes there to be some smooth scale-dependent function $f^{(N)}$, such that $\Delta E_{\max} = f^{(N)}(s)$. Without determining the form of that function, FSSA solves the best fit for a corresponding scale-invariant function $\tilde{f}$, such that $\Delta E_{\max} = N^{\zeta/\nu}\tilde{f}(N^{1/\nu}(s - s_c))$, by optimizing over the critical point s_c and critical exponents ζ, ν.

Because the smooth data are taken from the local minima of a nonsmooth plot, it is inhomogeneous. The values of s included in the dataset for one value of N are not the same as those of every other. For this reason, we approximate (s_c, ζ, ν) manually, finding the best fit in Fig. 14 with $s_c \approx 0.42$, $\zeta \approx 0.2$, and $\nu \approx 2$. However, note that this critical point lies well below the first oscillations in $\Delta E_{\max}$ at any system size. Solving the critical point and exponents with greater precision, and determining the relationship between the critical point and actual breakdown of QMBS, remains for future research.

[1] H. Lipkin, N. Meshkov, and A. Glick, Validity of many-body approximation methods for a solvable model: (I). Exact solutions and perturbation theory, Nucl. Phys. **62**, 188 (1965).

[2] M. Tavis and F. W. Cummings, Exact solution for an n-molecule—radiation-field Hamiltonian, Phys. Rev. **170**, 379 (1968).

[3] C. J. Turner, A. A. Michailidis, D. A. Abanin, M. Serbyn, and Z. Papić, Weak ergodicity breaking from quantum many-body scars, Nat. Phys. **14**, 745 (2018).

[4] A. N. Ivanov and O. I. Motrunich, Volume-entangled exact eigenstates in the PXP and related models in any dimension, Phys. Rev. Lett. **134**, 050403 (2025).

[5] E. Ising, Contribution to the theory of ferromagnetism, Z. Phys. **31**, 253 (1925).

[6] A. Russomanno, M. Fava, and M. Heyl, Quantum chaos and ensemble inequivalence of quantum long-range Ising chains, Phys. Rev. B **104**, 094309 (2021).

[7] H. Kim, T. N. Ikeda, and D. A. Huse, Testing whether all eigenstates obey the eigenstate thermalization hypothesis, Phys. Rev. E **90**, 052105 (2014).

[8] R. Mattes, I. Lesanovsky, and F. Carollo, Long-range interacting systems are locally noninteracting, Phys. Rev. Lett. **134**, 070402 (2025).

[9] A. Lerose, T. Parolini, R. Fazio, D. A. Abanin, and S. Pappalardi, Theory of robust quantum many-body scars in long-range interacting systems, Phys. Rev. X **15**, 011020 (2025).

[10] J. M. Deutsch, Eigenstate thermalization hypothesis, Rep. Prog. Phys. **81**, 082001 (2018).

[11] H. Bernien, S. Schwartz, A. Keesling, H. Levine, A. Omran, H. Pichler, S. Choi, A. S. Zibrov, M. Endres, M. Greiner, V. Vuletić, and M. D. Lukin, Probing many-body dynamics on a 51-atom quantum simulator, Nature (London) **551**, 579 (2017).

[12] M. Serbyn, D. A. Abanin, and Z. Papić, Quantum many-body scars and weak breaking of ergodicity, Nat. Phys. **17**, 675 (2021).

[13] M. Kac and C. J. Thompson, Critical behavior of several lattice models with long-range interaction, J. Math. Phys. **10**, 1373 (1969).

[14] D. Porras and J. I. Cirac, Effective quantum spin systems with trapped ions, Phys. Rev. Lett. **92**, 207901 (2004).

[15] H. Labuhn, D. Barredo, S. Ravets, S. de Léséleuc, T. Macrì, T. Lahaye, and A. Browaeys, Tunable two-dimensional arrays of single Rydberg atoms for realizing quantum Ising models, Nature (London) **534**, 667 (2016).

[16] J. Schachenmayer, B. Lanyon, C. Roos, and A. Daley, Entanglement growth in quench dynamics with variable range interactions, Phys. Rev. X **3**, 031015 (2013).

[17] P. Richerme, Z.-X. Gong, A. Lee, C. Senko, J. Smith, M. Foss-Feig, S. Michalakis, A. V. Gorshkov, and C. Monroe, Non-local propagation of correlations in quantum systems with long-range interactions, Nature (London) **511**, 198 (2014).

[18] J. Zhang, G. Pagano, P. W. Hess, A. Kyprianidis, P. Becker, H. Kaplan, A. V. Gorshkov, Z.-X. Gong, and C. Monroe, Observation of a many-body dynamical phase transition with a 53-qubit quantum simulator, Nature (London) **551**, 601 (2017).

[19] S. Pappalardi, A. Russomanno, B. Žunkovič, F. Iemini, A. Silva, and R. Fazio, Scrambling and entanglement spreading in long-range spin chains, Phys. Rev. B **98**, 134303 (2018).

[20] B. Žunkovič, M. Heyl, M. Knap, and A. Silva, Dynamical quantum phase transitions in spin chains with long-range interactions: Merging different concepts of nonequilibrium criticality, Phys. Rev. Lett. **120**, 130601 (2018).

[21] N. Defenu, A. Lerose, and S. Pappalardi, Out-of-equilibrium dynamics of quantum many-body systems with long-range interactions, Phys. Rep. **1074**, 1 (2024).

[22] M. H. Muñoz Arias, I. H. Deutsch, and P. M. Poggi, Phase-space geometry and optimal state preparation in quantum metrology with collective spins, PRX Quantum **4**, 020314 (2023).

[23] M. Heyl, F. Pollmann, and B. Dóra, Detecting equilibrium and dynamical quantum phase transitions in Ising chains via out-of-time-ordered correlators, Phys. Rev. Lett. **121**, 016801 (2018).

[24] R. Khasseh, A. Russomanno, M. Schmitt, M. Heyl, and R. Fazio, Discrete truncated Wigner approach to dynamical phase transitions in Ising models after a quantum quench, Phys. Rev. B **102**, 014303 (2020).

[25] M. H. Muñoz Arias, I. H. Deutsch, P. S. Jessen, and P. M. Poggi, Simulation of the complex dynamics of mean-field p-spin models using measurement-based quantum feedback control, Phys. Rev. A **102**, 022610 (2020).

[26] A. Mitra, T. Albash, P. D. Blocher, J. Takahashi, A. Miyake, G. W. Biedermann, and I. H. Deutsch, Macrostates vs. microstates in the classical simulation of critical phenomena in quench dynamics of 1D Ising models, New J. Phys. **27**, 013026 (2025).

[27] K. R. Chinni, Reliability of quantum simulation on NISQ-era devices, Ph.D. thesis, University of New Mexico, 2022.

[28] T. Comparin, F. Mezzacapo, and T. Roscilde, Robust spin squeezing from the tower of states of $u(1)$-symmetric spin Hamiltonians, Phys. Rev. A **105**, 022625 (2022).

[29] F. T. Arecchi, E. Courtens, R. Gilmore, and H. Thomas, Atomic coherent states in quantum optics, Phys. Rev. A **6**, 2211 (1972).

[30] R. Dicke, Coherence in spontaneous radiation processes, Phys. Rev. **93**, 99 (1954).

[31] L. Biedenharn and J. Louck, *Encyclopedia of Mathematics and Its Applications: Angular Momentum in Quantum Physics*, edited by G.-C. Rota (Addison-Wesley, Reading, MA, 1981), 2nd ed., Vol. 8.

[32] I. V. Protopopov, W. W. Ho, and D. A. Abanin, Effect of SU (2) symmetry on many-body localization and thermalization, Phys. Rev. B **96**, 041122 (2017).

[33] N. Debergh and F. Stancu, On the exact solutions of the Lipkin-Meshkov-Glick model, J. Phys. A: Math. Gen. **34**, 3265 (2001).

[34] H. Morita, H. Ohnishi, J. da Providência, and S. Nishiyama, Exact solutions for the LMG model Hamiltonian based on the Bethe ansatz, Nucl. Phys. B **737**, 337 (2006).

[35] A. B. Klimov and J. L. Romero, A generalized Wigner function for quantum systems with the SU (2) dynamical symmetry group, J. Phys. A: Math. Theor. **41**, 055303 (2008).

[36] A. B. Klimov, J. L. Romero, and H. de Guise, Generalized SU (2) covariant Wigner functions and some of their applications, J. Phys. A: Math. Theor. **50**, 323001 (2017).

[37] A. Lerose, B. Žunkovič, J. Marino, A. Gambassi, and A. Silva, Impact of nonequilibrium fluctuations on prethermal dynamical phase transitions in long-range interacting spin chains, Phys. Rev. B **99**, 045128 (2019).

[38] K. Chinni, P. M. Poggi, and I. H. Deutsch, Effect of chaos on the simulation of quantum critical phenomena in analog quantum simulators, Phys. Rev. Res. **3**, 033145 (2021).

[39] Z. Li, A. Delmonte, X. Turkeshi, and R. Fazio, Monitored long-range interacting systems: Spin-wave theory for quantum trajectories, Nat. Commun. **16**, 4329 (2025).

[40] U. Schollwöck, The density-matrix renormalization group in the age of matrix product states, Ann. Phys. **326**, 96 (2011).

[41] J. Schachenmayer, A. Pikovski, and A. M. Rey, Many-body quantum spin dynamics with Monte Carlo trajectories on a discrete phase space, Phys. Rev. X **5**, 011022 (2015).

[42] J. Haegeman, C. Lubich, I. Oseledets, B. Vandereycken, and F. Verstraete, Unifying time evolution and optimization with matrix product states, Phys. Rev. B **94**, 165116 (2016).

[43] W. J. Eckner, N. Darkwah Oppong, A. Cao, A. W. Young, W. R. Milner, J. M. Robinson, J. Ye, and A. M. Kaufman, Realizing spin squeezing with Rydberg interactions in an optical clock, Nature (London) **621**, 734 (2023).

[44] G. Bornet, G. Emperauger, C. Chen, B. Ye, M. Block, M. Bintz, J. A. Boyd, D. Barredo, T. Comparin, F. Mezzacapo, T. Roscilde, T. Lahaye, N. Y. Yao, and A. Browaeys, Scalable spin squeezing in a dipolar Rydberg atom array, Nature (London) **621**, 728 (2023).